T.R.

GEBZE TECHNICAL UNIVERSITY

GRADUATE SCHOOL OF NATURAL AND APPLIED SCIENCES

INVESTIGATION OF SPIN-GAPLESS MATERIALS: A FIRST PRINCIPLES DFT+GW STUDY

KÜBRA NUR KALKAN

A THESIS SUBMITTED FOR THE DEGREE OF

MASTER OF SCIENCE

PHYSICS DEPARTMENT

GEBZE

2023

T.K.

GEBZE TECHNICAL UNIVERSITY

GRADUATE SCHOOL OF NATURAL AND APPLIED SCIENCES

INVESTIGATION OF SPIN GAPLESS MATERIALS: A FIRST PRINCIPLES DFT + GW STUDY

KÜBRA NUR KALKAN

A THESIS SUBMITTED FOR THE DEGREE OF MASTER OF SCIENCE

DEPARTMENT OF PHYSICS

THESIS SUPERVISOR

PROF. DR. MURAT TAŞ

GEBZE

2023

T.C.

GEBZE TEKNİK ÜNİVERSİTESİ

FEN BİLİMLERİ ENSTİTÜSÜ

SPİN BOŞLUKSUZ MALZEMELERİN İNCELENMESİ: İLK PRENSİPLER DFT+GW ÇALIŞMASI

KÜBRA NUR KALKAN

YÜKSEK LİSANS TEZİ

FİZİK BÖLÜMÜ ANABİLİM DALI

TEZ DANIŞMANI

PROF. DR. MURAT TAŞ

GEBZE

2023

GEBZE TEKNİK ÜNİVERSİTESİ	**YÜKSEK LİSANS JÜRİ ONAY FORMU**

GTÜ Fen Bilimleri Enstitüsü Yönetim Kurulu'nun 19/07/2023 tarih ve 2023/40 sayılı kararıyla oluşturulan jüri tarafından 18/08/2023 tarihinde tez savunma sınavı yapılan Kübra Nur Kalkan'ın tez çalışması Fizik Anabilim Dalında YÜKSEK LİSANS tezi olarak kabul edilmiştir.

JÜRİ

ÜYE
(TEZ DANIŞMANI) : PROF. DR. MURAT TAŞ

ÜYE : PROF. DR. SAVAŞ BERBER

ÜYE : PROF. DR. MUSTAFA SARISAMAN

ONAY

Gebze Teknik Üniversitesi Fen Bilimleri Enstitüsü Yönetim Kurulu'nun

...../...../..... tarih ve ...../..... sayılı kararı.

İMZA/MÜHÜR

SUMMARY

Spintronics devices, which are based on the spin properties of electrons as well as their charges, are important alternative to the electronic devices in developing technology. In this context spin-gapless semiconductors (SGSs) are considered as one of the most promising candidates with their unique electronic band structures. This thesis focuses on investigation of new SGSs via first-principles calculations. We studied several quaternary Heusler alloys for our investigations: FeVNbAl, FeCrTiAl, FeCrZrAl, NiCrMnAl and NiFeMnAl. These materials were already predicted to show SGS behaviour in previous studies. We computed the electronic band structure of selected materials within the framework of well-established density functional theory (DFT) and *GW* approximation. In a two-stage calculation, we investigated whether these materials have SGS properties, and compared the results of two methods.

Key Words: Spintronics, Spin-gapless materials, First-principles calculations, DFT, *GW* approximation

ÖZET

Elektronların hem yüklerini hem de spin özelliklerini kullanan spintronik cihazlar, gelişen teknolojide geleneksel elektronik cihazlara önemli bir alternatif oluşturmaktadır. Bu bağlamda, spin-gapless yarı iletkenler (SGS), benzersiz elektronik bant yapılarıyla en umut verici adaylardan biri olarak kabul edilmektedir. Bu tez, ilk prensip hesaplamaları yoluyla yeni SGS malzemelerin araştırılmasına odaklanmıştır. Araştırmalarımız için dört elementli Heusler alaşımı üzerinde çalıştık: FeVNbAl, FeCrTiAl, FeCrZrAl, NiCrMnAl and NiFeMnAl. Bu malzemelerin SGS davranışı göstereceği önceki çalışmalarda tahmin edilmişti. Oldukça iyi bilinen yoğunluk fonksiyonel teorisi (DFT) ve *GW* yaklaşımlarını kullanarak seçilen malzemelerin elektronik bant yapısını hesapladık. İki aşamalı bir hesaplamada bu sistemlerin SGS özelliklerine sahip olup olmadığını araştırarak iki yöntemin sonuçlarını karşılaştırdık.

Anahtar Kelimeler: Spintronik, Spin-aralıksız malzemeler, İlk prensipler hesaplamaları, DFT, *GW* yaklaşımı

ACKNOWLEDGEMENTS

First of all, I would like to thank my advisor, Prof. Dr. Murat Taş, for his unfailing support and being an excellent guide. Also, his indulgence of my mistakes kept me highly motivated throughout the research.

Also, my mum, my dad, my sisters and my bro-in-law… I owe everything to their unconditional trust, support and love for me. I am thankful to them for letting me fly in my own sky and endless thanks to my family for being in at my journey.

I would love to thank my friends, with whom I share all my experiences, good or bad, while doing the job I love the most, and who have been consistent sources of joy in my life.

Finally, I feel gratitude to Prof. Dr. Savaş Berber who helped me solve some problems I faced during my simulations on the TRUBA clusters by giving on-point advice. Also, I would like to thank Prof. Dr. Mustafa Sarısaman who was one of the members of the MS thesis jury.

The numerical calculations reported in this thesis were fully performed at TUBITAK ULAKBIM, High Performance and Grid Computing Center (TRUBA resources).

This thesis and all my future works are dedicated to my beloved Turkish flag, which enhances my determination to work every single day, my family who never stop believing in me, and my friends who make me proud with their achievements.

TABLE OF CONTENTS

LIST OF ABBREVIATIONS AND ACRONYMS

Abbreviations and Acronyms		Explanations
μ_B	:	Bohr Magneton
E_F	:	Fermi Energy
O_h	:	Octahedral Site Symmetry
T_d	:	Tetrahedral Site Symmetry
APW	:	Augmented Plane Wave
DFT	:	Density Functional Theory
DMS	:	Dilute Magnetic Semiconductor
DSGS	:	Dirac Spin Gapless Semiconductor
FET	:	Field Effect Transistor
FCF	:	Fully Compensated Ferrimagnet
DFT	:	Full-Potential Linearized Augmented Plane Wave
GGA	:	Generalized Gradient Approximation
GMR	:	Giant Magnetoresistance
HDD	:	Hard Disk Drive
HMF	:	Half-Metallic Ferromagnets
IC	:	Integrated Circuit
LAPW	:	Linearized Augmented Plane Wave
LDA	:	Local Density Approximation
Meta-GGA	:	Meta Generalized Gradient Approximation
MPB	:	Mixed Product Basis
PSGS	:	Parabolic Spin Gapless Semiconductor
RAM	:	Random Access Memory
RPA	:	Random Phase Approximation
SGS	:	Spin Gapless Semiconductor

LIST OF FIGURES

LIST OF TABLES

1 INTRODUCTION

In modern technology, electronic devices used in our daily life are mostly based upon the charge of electrons. An integrated circuit (IC) consisting of large amount of components such as transistors is one of the main elements of modern electronics. Transistors control the flow of electric charge, or the electric current, in an IC [1]. A conventional transistor such as a field effect transistor (FET) has four regions: gate, source, drain and channel [2]. When there is no applied voltage to the gate, there will be no flow of electric current and thus we have an off-state, or “0”. Conversely, when there is a voltage applied to the gate terminal, the electrons move through the transistor and the transistor flips to on-state or “1”. This is how data is stored and processed conventionally.

It can be considered that the modern information age began in the late 1950’s. Nobel laureate Jack Kilby designed the first integrated circuit in 1958 and he filed a patent for his invention called "Miniaturized Electronic Circuit" in 1959 [3]. Microelectronics technology has enabled devices with more complicated data stored on a smaller area. Moreover, the compactness of ICs brings about not only less production cost but also faster signal transmission. Therefore, the main focus of this technology evolved around storing more information on smaller area with less production cost. When electronics with ICs was in its infancy, Gordon E. Moore, co-founder of Intel Corporation, published an article emphasizing the importance of ICs and pointing out how semiconductors would be a key point for microelectronics technology in near future [4]. In his article in 1965, Moore stated his predictions about next ten years of electronics centred around the ICs under the claim of smaller and faster devices with lower costs. In addition to these statements, Moore’s Law was mentioned for the first time in the article. According to the first version of Moore's law, the number transistors on a microchip would double every year between 1965-1975 [5] .

Taking into account the ten-year period with the first version of Moore’s law, the complexity of ICs was doubled annually. Doubling the number of transistors on the same amount of area implied that transistors had to get much smaller each year. In other words, density of ICs was expected to increase exponentially each year. While increasing the complexity of ICs, safe functionality of electronic devices and

capabilities of the semiconductor industry had to be considered for the sake of a sustainable growth in microelectronics technology. Considering those factors, Moore updated his predictions on the growth of microelectronics technology in 1975 [4]. He stated that the number of electronic components per microchip would double every two years, instead of doubling every year [6]. Figure 1-2 shows how the number of components per chip was predicted to increase over the years by Moore's Law of 1975 [6].

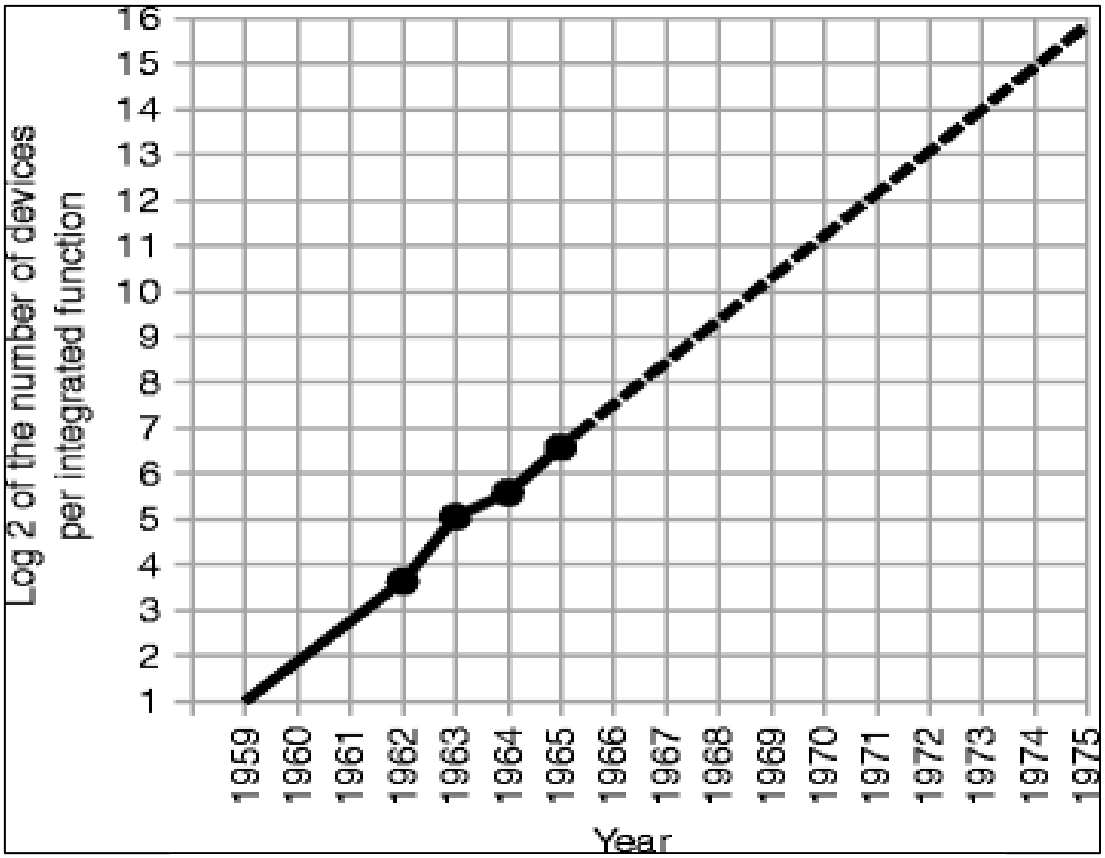

Figure 1.1Moore's Law, 1965.

Indeed, the evolution of electronic technology has actualized as predicted by Moore's law: the number of transistors per chip doubles approximately every two years. To illustrate how exponentially the growth has been, it is enough to look at the number of transistors per chip for Intel 286 produced by Intel Corporation in 1982, and M2 Max by Apple Inc. in 2023. While Intel 286 processor had 134.000 transistors, M2 Max has 67.000.000.000 electronic components [7,8]. Although there is no yet a conflict between the Moore's law and physical laws regarding the miniaturization of components in electronic devices, there is no way to ignore the physical limits of semiconductor-based transistors.

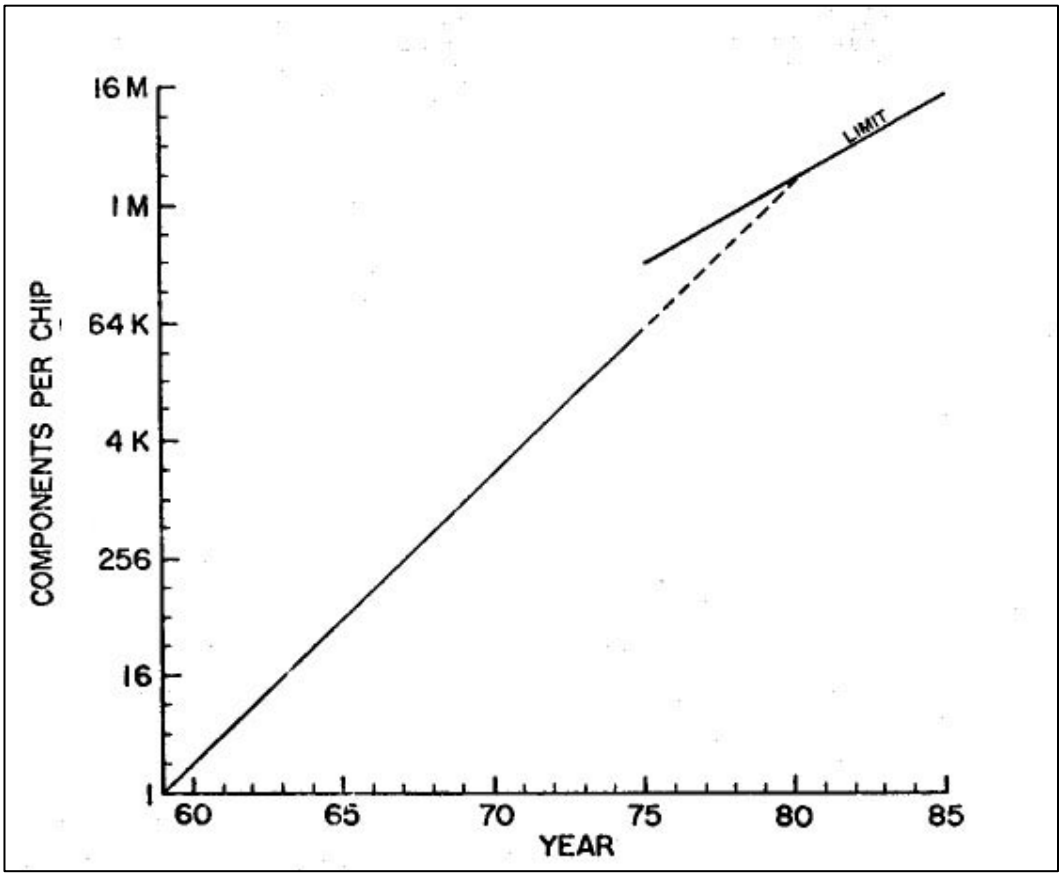

Figure 1.2 Projection of the complexity curve reflecting the limit on increased density through invention, 1975.

The question is whether semiconductor-based transistors will continue to keep up with supply and demand equilibrium in modern technology. To understand the properties which prospect materials must have, it would be helpful to touch on the challenges that current electronics will face in near future.

Two branches of physics set limits on further shrinking of transistors: quantum mechanics and thermodynamics. As transistors get shrunk, terminals inside a transistor come closer to each other and thickness of the insulator between the channel and gate is decreased. When the size of a transistor is not small enough for quantum effects to take control, there exists an electric field due to the depletion layer between the n-type and p-type semiconductors [9]. This implies electric field in the channel prevents the electron flow from the source to drain and the transistor is in the off state. At a point where length of the channel and thickness of the insulator come down to atomic scales, quantum mechanics comes into play with wave-particle duality. Making analogy to potential barrier problem, wave-like electrons can flow into the other side even if the

transistor is in the off-state, *i.e.*, quantum tunnelling [10]. As a consequence of the quantum nature of electrons, there occurs current leakage in the circuit [10,11]. Besides, the exponential increase in the number of transistors pushes the limits of the laws of thermodynamics after a critical point. The main limitation in this regard is that dissipated power must remain at an acceptable value [12,13]. As the electric field strength is reduced, electric current flows through the transistor [1]. Even without including the miniaturization of transistors, some amount of heat is already generated during switching the states and flowing current inside the wires [14]. Although the energy needed for devices has been inversely proportional to the number of transistors in ICs, it is expected that energy consumption will increase the production costs of electronics in near future. The denser the integrated circuits are, the more problems about taking control over power consumption in devices become [15]. This leads to an increase in heat production and therefore a decrease in efficiency.

Particularly taking into account the physical and economic constraints, the inevitable need for a new technology emerges. One of the most feasible steps for new breakthroughs is to change the methods of storing and processing of data. As it is stated above, electronics utilizes the charge of electrons for transmitting, processing and storing information. In addition to charge and mass, electrons also have an intrinsic angular momentum, the spin, which is a purely quantum mechanical property [16,17].

1.1 Spintronics

In spin magnetic moment-based electronics, or shortly spintronics, the spin of electrons is used as the information carrier. Spintronic devices date back to the 1950's. In 1953, Magnetic Core Memory (MCM) consisting of magnetic rings was developed at MIT [18]. Each ring-shaped magnetic material was considered as a bit, and their magnetization direction was represented either “1” or “0” [19]. The MCM became the first Random Access Memory (RAM). In the late 1980’s, Albert Fert and Peter Grünberg discovered the Giant Magnetoresistance (GMR) in a structure made up of a non-magnetic metal between two ferromagnetic materials [20,21]. By applying magnetic field, they managed to manipulate magnetic orientations of ferromagnetic layers [22]. The state “1” or “0” is read according to their parallel or antiparallel

alignments to each other, respectively. One of the most popular applications of GMR is Hard Disk Drive (HDD), which was mostly used in computers until 15 years ago.

The ultimate goal in spintronics is to extend the point reached in electronic devices by adding the electron's spin degree of freedom. Since the spin magnetic moment is an instinctive property, the power needed for storing and transporting information is alleviated correspondingly. When electric current flows through a non-magnetic metal, the scattering of electrons is independent of their spin states. This means that there are equal numbers of electrons with spin-up and spin-down states, and net current is unpolarized charge current [23]. However, when electrons move through a ferromagnetic material, spin-up and spin-down electrons scatter somehow at different rates, and there occurs a net spin polarized current [24]. In other words, unpolarized electric current becomes spin polarized in ferromagnetic materials. Thanks to the interaction between the spin and magnetic field, spin polarized current can be manipulated easily [25,26]. Spin polarization results in different conductivity for spin-up and spin-down currents [23,26]. Hence, two spin states represent two different channels. Transporting information by spin current enables devices to dissipate less power, to process data faster, to be more reliable and non-volatile [25]. The more spin polarization a material has around the Fermi energy level, the more suitable it becomes for spintronics applications. Materials that are suitable for spintronics can be sorted by their energy band diagrams. Having fully spin polarized band structure, spin gapless semiconductors (SGSs) under the category of magnetic semiconductors, and half-metal (HM) subgroup of magnetic metals promise great hopes for spintronic devices [27] .

1.2 Motivation and Purpose

In the digitized world the demands for accessing, storing and fast processing the information are increasing exponentially day by day. Seeking a way to solve the problems faced with conventional electronic devices in near future is the motivation for this thesis. In this context, we chose the SGSs for our research. Our reasoning for this choice will be clear in the next section.

This thesis focuses on the investigation of new semiconductors which are predicted to be spin-gapless by employing state-of-art software based the DFT and *GW* approximation. Our selection criteria for materials are that they can be synthesized and are suitable for use in daily life. In this direction, we took into account their mechanical and thermodynamic stability, and ability to maintain their magnetic property and spin polarized energy band structure close to room temperatures. Our methodology and studied materials will be detailed in the following chapter.

2 SPIN-GAPLESS SEMICONDUCTORS

Magnetic materials keep drawing immense attention of researchers due to their magnetic and electronic properties for device applications. Magnetic semiconductors and half-metallic ferromagnets (HMF) are known as some of the most promising types of materials that have been investigated in many theoretical and experimental studies. For practical and realistic applications, a material has to keep its magnetic order around room temperature and should have high-spin polarization around Fermi energy level [27]. In this context, magnetic semiconductors such as dilute magnetic semiconductors (DMS) may not be the most suitable material type due to their quite low Curie temperature T_c [28]. On the other hand, half-metallic ferromagnets (HMF), proposed by de Groot *et. al.* in 1983, have high T_c and, thus, preserve their magnetic property at near room temperatures [29]. Their electronic band structure is 100% spin polarized meaning that one spin channel with metallic behaviour and the other with semiconducting property [30]. In 2008, Xiaolin Wang came up with another class of materials, the spin-gapless semiconductors (SGSs) [31]. In his proposal, not only the concept of SGSs was introduced but also cobalt doped $PdPbO_2$ was presented as the first SGS [31]. With their unique electronic band structures, SGSs have been one of the popular candidates for spin-based electronics for fifteen years. Mn_2CoAl, an inverse Heusler compound, was experimentally verified as the first SGS in 2013 [32]. The electronic band structure of SGSs shows two different material properties with two independent spin channels [31–33]. In one spin channel, there is an energy gap between the valence and conduction bands, while top of the valence band and bottom of the conduction band touch around Fermi energy in the other spin channel [31–34]. No gap implies that charge carries, electrons and/or holes, do not need any energy for excited from valence band to conduction band [31–35]. Before going into details about types of the SGSs, it would be useful to mention their basic features that make them desirable.

- No energy is needed to move electrons from valence band to conduction band owing to having zero gap in one of the spin channels.
- They have high Curie temperature T_c .
- Both holes and electrons can have 100% spin polarization.

- It is easy to separate fully spin-polarized charge carriers from each other by spin filtering.
- They have nearly temperature-independent and low carrier concentration.
- They have nearly temperature-independent and low conductivity, almost zero around Fermi energy E_F as a result of almost zero density of states (DOS).
- They have rather a small Seebeck coefficient [31–37].

As a result of the gapless or narrow-gap nature in one spin channel, the SGSs are so sensitive to external effects that charge carriers and their spin states can be manipulated by little effort, like with small pressure or electric field [37,38] .

According to the energy-momentum dispersion relations, they can be classified into parabolic or linear SGSs [31,34,35] . Under each class, there are four types of SGSs with respect to the behaviour of spin channels around E_F.

2.1 Parabolic SGSs

According to spin polarization of their valence band (VB) and conduction band (CB), the parabolic SGSs (PSGSs) are classified as follows [31,33,35].

Type-I**:** Both VB and CB touch at Fermi level for spin-up channel. However, there is a gap between the bands for spin-down channel (see Figure 2.1a).

Type-II: Both spin channels have a gap, but top of the VB in spin-up channel touches the CB bottom in spin-down channel at E_F implying that both spin channels make contribution to gapless nature of the material (see Figure 2.1b).

Type-III: There is no gap in spin-up channel, and bottom of the CB in spin-down channel also touches E_F (see Figure 2.1c).

Type-IV: There is no gap in spin-up channel, and top of the VB in spin-down channel also touches Fermi energy (see Figure 2.1d) [33,36].

Noting that the articles by Gao *et al.* and Rani *et al.* are also cited here, although the numbering of types may vary in them.

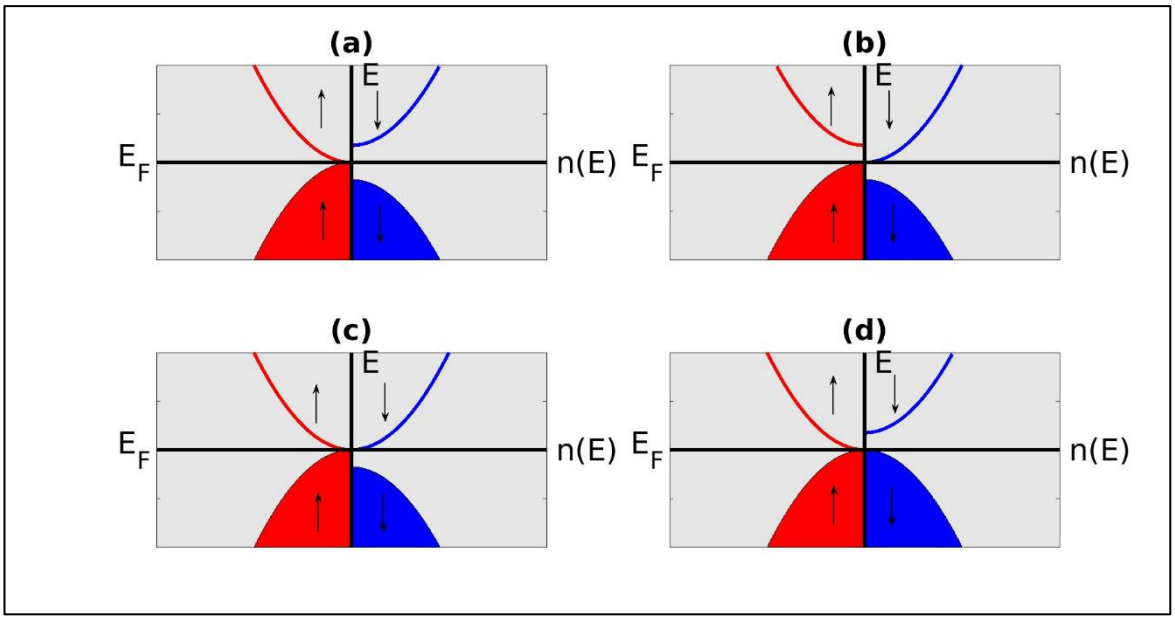

Figure 2.1: Types of parabolic spin gapless semiconductors (PSGSs)

Wang introduced the concept of SGSs because of theoretical calculations on $PbPdO_2$ using the DFT [31]. He verified $PbPdO_2$ as the first oxide-based gapless semiconductor which is non-magnetic. Then he obtained the first SGS from pure $PbPdO_2$ by doping Co atom for one Pd in a unit cell [39]. Co-doped $PbPdO_2$ has the energy band diagram configuration corresponding to Type-II. In 2009, spin-gapless semiconducting behaviour of Co-doped $PbPdO_2$ was experimentally verified. A lot of theoretical research has been done on PSGSs. For instance, diamond-like quaternary compound $CuMn_2InSe_4$ (3D) and CO-Mn-g-ZnO (2D) have been predicted as PSGS using first principles calculations [40,41]. Considering both theoretical and experimental research done so far, Heusler compounds with high T_c and easy to be synthesized are the most promising candidates in the search for SGSs [35].

2.1.1 Full-Heusler Based SGSs

Full-Heusler compounds with X_2YZ chemical formula, or Cu_2MnAl-type alloys, belong to Fm-3m (225) 3D space group under cubic crystal system [42]. Ternary Heusler alloys with X_2YZ crystallizing in $L2_1$ structure are composed of four face-centred cubic sublattices [30,43,44]. The unit cell consists of four atoms, three of which are different. X and Y atoms are in the transition metal (TM) group while Z is

the main group element, so-called sp atom. For ternary Heusler compounds with the basis X-Y-X-Z, the Wyckoff positions are (0,0,0), (¼, ¼, ¼), (½, ½, ½) and (¾, ¾, ¾), respectively [30,43–46]. When the atomic number of Y is greater than that of X, the ternary Heusler compounds with X_2YZ formula crystallize in X_A structure, or Hg_2CuTi-type, and they are named inverse Heusler compounds [43]. The sequence of atoms' occupation for the most energetically stable inverse Heusler alloys is X-X-Y-Z with (0,0,0), (¼, ¼, ¼), (½, ½, ½) and (¾, ¾, ¾), respectively [43,47].

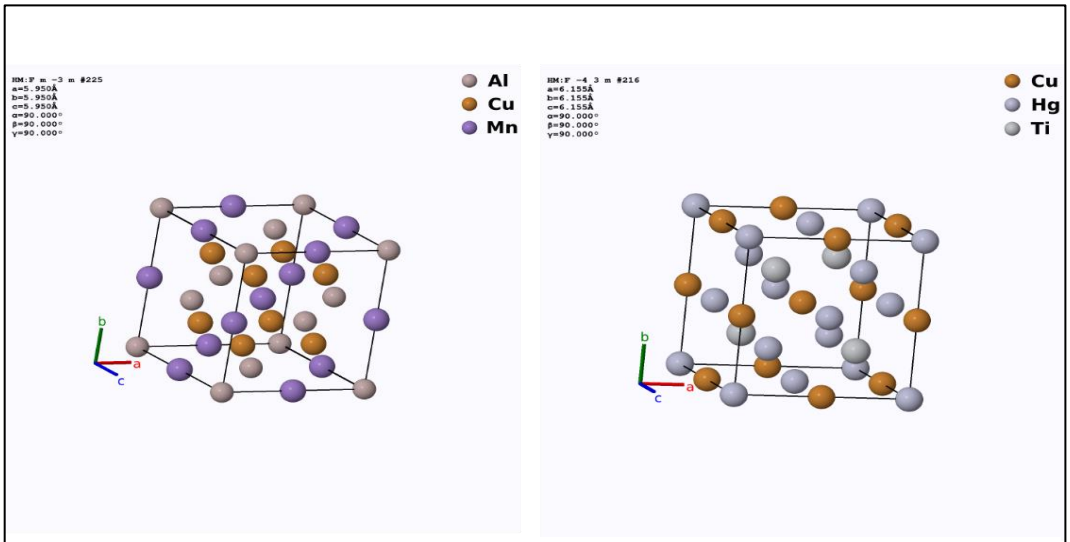

Figure 2.2: Full-Heusler Prototype (left). Inverse Heusler Prototype (right).

Figure 2.2 shows full-Heusler and inverse Heusler prototypes [48–50]. The symmetry positions that atoms have, due to their occupation and interaction of atoms with their neighbours, play a crucial role for interpreting energy band structure of the full-Heusler compounds. Interactions between atomic orbitals, specifically d orbitals, also affects magnetic properties of the material. As with half-metals, in the case of full-Heusler based SGS the net magnetic moment per unit cell is an integer, and it obeys the Slater-Pauling rule [46].

$$N_v = N_\uparrow + N_\downarrow \quad , \qquad 2.1$$

where N_v is the total number of valence electrons in the unit cell, and

$$M_\Sigma = N_\uparrow - N_\downarrow, \qquad 2.2$$

where M is net magnetic moment. Then, $M_\Sigma = (N_v - N_\downarrow) - N_\downarrow \Rightarrow M_\Sigma = N_v - 2N_\downarrow$ [51,52]. Relation M = Z - 2N holds for Heusler alloys in general.

In Heusler-based SGSs, minority, or spin-down, spin channel displays semiconducting behaviour, while the valence and conduction bands of majority, or spin-up, spin channel touch each other at the Fermi level [46]. According to the Slater-Pauling behaviour, the number of valence electrons in the minority spin channel is fixed, and net magnetization per unit cell depends on the occupied states of spin-up channel [30,43].

In the full-Heusler compounds, both Y and Z atoms have octahedral (O_h) site symmetry with eight X atoms as the nearest neighbours. While X atoms have four Y and four Z atoms as the nearest neighbours making their site symmetry to be tetrahedral [30,36,44]. Hence the symmetry that crystal has is also tetrahedral (T_d) crystallographic symmetry [30,44]. It is important to note that splitting in d orbitals is the same for two symmetry positions: two-fold degenerate e_g and three-fold degenerate t_{2g}, with the only difference that energy of the two-fold degenerate orbitals is higher in O_h and lower in T_d than energy of the three-degenerate ones [53]. Although X atoms are second-degree neighbours with each other, the hybridization between their d-orbitals is taken account first due to the gap formed between the two of resultant hybrids and the magnetic moment arising from their interaction [30,46,54]. The sites where X atoms sit with respect to each other have O_h symmetry. Splitting d-orbitals under O_h results in two-fold degenerate (e_g) and three-fold degenerate (t_{2g}) orbitals with energies $E(e_g) > E(t_{2g})$ [55]. As a result of X-X hybridization, there occurs 5 bonding and 5 anti-bonding hybrid orbitals: $2e_g$, $3t_{2g}$, $3t_{1u}$, $2e_u$. Then the hybrids interact with d-orbitals of Y atom that they obey the same symmetry transformation. After the second hybridization, there exists 5 bonding and 5 anti-bonding orbitals in addition to 5 non-bonding orbitals obtained from the first hybridization. The Fermi level is located between two non-bonding orbitals [56]. Now we can adopt the Slater-Pauling rule for full-Heusler compounds since all occupied minority states are determined. Number of filled states in the minority spin channel is 12, of which 4 are from 3p and 1s orbitals, and 8 are from hybrids orbitals below the Fermi level [30]. Hence, the Slater-Pauling behaviour of full-Heusler compounds is $M_t = N_v - 24$. There

occurs splitting into the minority and majority spin channels due to the exchange interaction between electrons. As a result of the spin splitting, energy levels of hybrids in the majority spin channel are shifted without changing their corresponding symmetry representation and total number of energy levels [57]. While the minority spin channel has semiconducting behaviour, the majority spin channel has no gap, and its highest state in the valence band touches its lowest state in the conduction band at the Fermi energy level.

For the inverse Heusler compounds to have SGS behaviour, there are three possible Slater-Pauling rules according to the sites their atoms are located in the unit cell. Skaftouros stated that the cases X=Ti (Ti-based), X= Cr or Mn with Y= Cu or Zn satisfy the Slater-Pauling behaviour $M_t = N_v - 18$, $M_t = N_v - 24$, and $M_t = N_v - 28$, respectively [58]. Hybridization process of inverse Heusler (Hg_2CuTi-type) alloys is similar to the case of the Cu_2MnAl-type. For the case of X=Ti, Ti atom located at 4a site interacts with the other atom having the same symmetry position which is Y atom at 4b site in the X_A structure. Then, 5 bonding and 5 anti-bonding orbitals are formed, as in the first interaction in the $L2_1$ structure [47,58]. Secondly, bonding orbitals formed by Ti(1)-Y hybridization interact with d-orbitals of the other Ti atom at 4c site with corresponding symmetry positions. The Fermi energy level is between t_{1u} non-bonding states and t_{2g} bonding states. Thus, total number of occupied states in the minority spin channel is 9 [47,58]. The second case for which X=Cr or Mn, the occupancy of minority spin states and gap formation are the same as in the full-Heusler compounds, which means that the number of filled states in the minority spin channel is 12 [58–60]. In the last case where X=Cr or Mn and Y=Zn or Cu, hybridization occurs only between X atoms, and the gap is formed in between the lowest anti-bonding orbitals and the highest bonding orbitals. The d-orbitals of Y atom are fully occupied, thus the total number of filled states in the minority spin channel is 14 [58–61].

Thanks to the Slater-Pauling rules, magnetic classification of Heusler-based SGSs can be determined. If the number of spin-down valence electrons is equal to the number of spin-up valence electrons in the unit cell, then the net magnetization in the unit cell becomes zero. This implies that the material is fully compensated ferrimagnetic SGS [59]. For the ferromagnetic inverse Heusler-based SGS, candidates should have N_V=21 (9 spin-down, 12 spin-up), 26 (12 spin-down, 14 spin-up) [46].

Table 2.1 shows a group of inverse Heusler compounds that show SGS behaviour [32,47,59,62,63].

Table 2.1: A group of inverse Heusler compounds showing SGS behaviour

Compound	a (Å)	M_{tot} (μ_B)	N_V	Magnetic Type
Ti_2MnAl	6.24	0	18	FCF
Ti_2MnGa	6.21	0	18	FCF
Ti_2CoSi	6.03	3	21	Ferromagnetic
Mn_2CoAl	5.798	2	26	Ferromagnetic
Cr_2ZnSi	5.85	0	28	FCF

2.1.2 Quaternary Heusler-Based SGSs

Quaternary Heusler (QH) compounds with XX'YX chemical formula, so-called LiMgPdSn-type or Y-type, structure belong to the F-43m space group (#216) under the cubic crystal system with four interpenetrating fcc sublattices [37]. There are four different atoms in a unit cell; X, X', Y are TM and Z atom is the main group element [64,65]. The number of valence electrons of atoms follows the rule: $N_V(Y) < N_V(X') < N_V(X)$ [64–66]. There are three available crystal structures obtained by the occupation of Z atom being fixed at 4d site [36,64,65]. For type-1, type-2 and type-3 the X atom occupies 4a, 4a and 4c sites, the X' atom does 4b, 4c and 4b sites and the Y atom is located at 4c, 4b and 4a sites, respectively [36,64,65]. As electronic and magnetic properties of compounds are described by the interaction between atoms in the unit cell and which sites they occupy, the stability of QH alloys varies relying on their structural types. Like all other half-metallic and SGS Heusler materials, the Slater-Pauling rule is satisfied by quaternary SGS Heusler. Compounds with N_V=21 obey $M_t = N_v - 18$, and

the ones with N_V=26 or N_V=28 obey $M_t = N_v - 24$ rules [36,66]. Considering minimum total energy as a function of site occupation, in other words, energetically stable crystal structure XX'YZ with 4a, 4b, 4c, and 4d in the respective order is the most stable structure [67]. Here, the Slater-Pauling behaviour of QH alloys is taken

into account based on these occupations at the sites. In these compounds, X, X', Y and Z atoms have the same site symmetry which is tetrahedral T_d site symmetry [36]. In the tetrahedral crystal field, d-orbital splitting brings about two-fold degenerate (e_g) states and three-fold degenerate (t_{2g}) states as in the octahedral O_h site symmetry. represents the quaternary Heusler prototype [48–50] .

Like all other half-metallic and SGS Heusler materials, the Slater-Pauling rule is satisfied by quaternary SGS Heusler. Compounds with N_V=21 obey $M_t = N_v - 18$, and

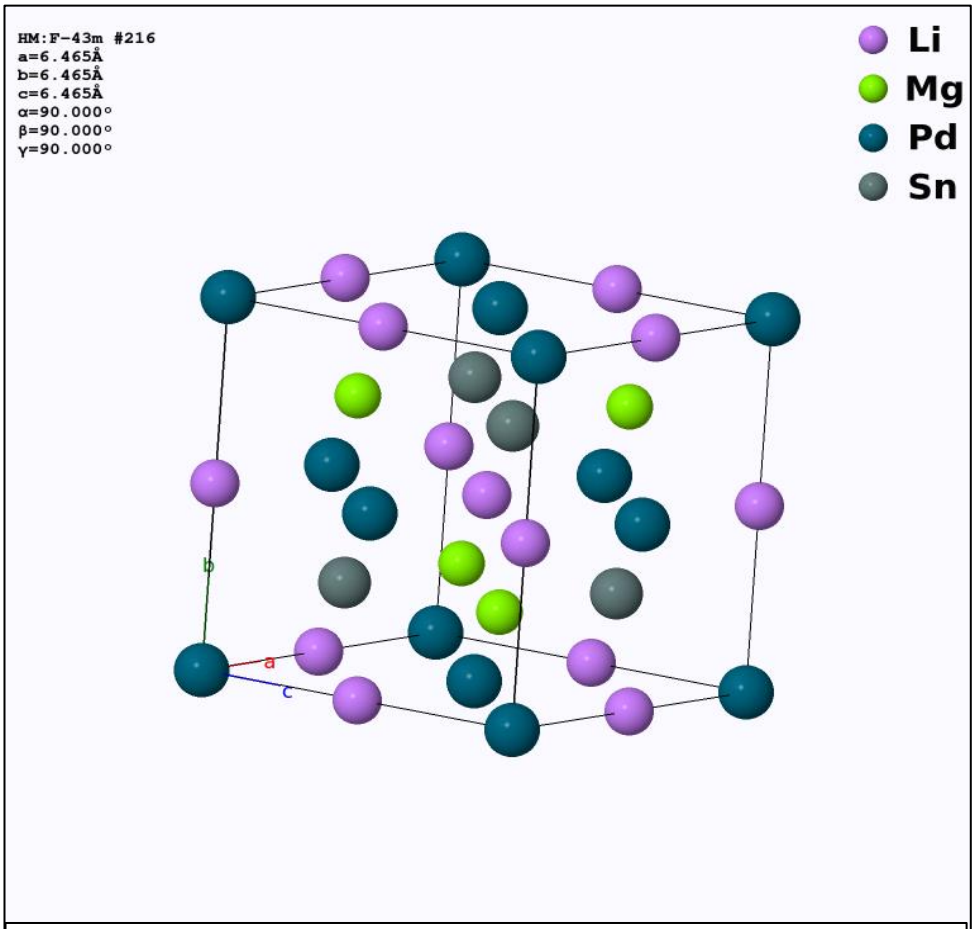

Figure 2.3: Quaternary Heusler protype

the ones with N_V=26 or N_V=28 obey $M_t = N_v - 24$ rules [36,66]. Considering minimum total energy as a function of site occupation, in other words, energetically stable crystal structure XX'YZ with 4a, 4b, 4c, and 4d in the respective order is the most stable structure [67]. Here, the Slater-Pauling behaviour of QH alloys is taken into account based on these occupations at the sites. In these compounds, X, X', Y and Z atoms have the same site symmetry which is tetrahedral T_d site symmetry [36]. In the tetrahedral crystal field, d-orbital splitting brings about two-fold degenerate (e_g)

states and three-fold degenerate (t_{2g}) states as in the octahedral O_h site symmetry. The energy value of e_g states is lower than that of t_{2g}, while (e_g)'s energy is higher than (t_{2g}) energy value in the octahedral crystal field [55].

To begin with, d-orbitals of X atom at 4a(0,0,0) and X' atom at 4b(½, ½,½) hybridize [57]. This d-orbital hybridization between X-X' atoms brings along 5 bonding orbitals: $2e_g$ and 3 t_{2g} and 5 anti-bonding orbitals: $3t_{1u}$ and $2e_u$. Then, bonding orbitals couple with d-orbitals of Y atom which are also split into three-fold degenerate states and two-fold degenerate states [36,57]. As a result of the second interaction between X-X' and Y atoms, 5 bonding: $2e_g$ and 3 t_{2g} and 5 anti-bonding: $2e_g$ and $3t_{2g}$ orbitals occur. Due to having difference in symmetry representation, anti-bonding orbitals $3t_{1u}$ and $2e_u$ resulted by X-X' hybridization do interact with d-orbitals of Y atom [36,53]. Interaction between the nearest neighbours and hybridization resulting in gap formation are similar to full-Heusler and inverse Heusler alloys. For the case of N_V=21, a gap is formed between occupied bonding three-fold orbitals and unoccupied non-bonding three-fold states in the minority spin channel [66]. This implies that the number of valence electrons with down spin state is 9. In the majority spin channel, the highest occupied level, and the lowest unoccupied level meet at the Fermi energy level [36,46,66]. For the cases of N_V=26 and N_V=28, the number of valence electrons in their minority spin-down states is 12. Thus, non-bonding states (t_{1u}) are occupied, and Fermi level is located between the e_u and t_{1u} states [57,58,66]. Valence electrons with up spin state determine their magnetic property. In Table 2.2, a group of QH alloys which have SGS behaviour is listed [33,37,62,66,68].

Table 2.2: A group of Quaternary Heusler compounds showing SGS behaviour.

Compound	a (Å)	M_{tot} (μ_B)	N_V	Magnetic Configuration
CrVTiAl	6.20	-0.04	18	FCF
CoVTiAl	6.04	3.0	21	Ferromagnetic
CoFeTiAl	5.81	0.0	24	FCF
CoFeMnSi	5.62	4.0	26	Ferromagnetic

2.1.3 Half-Heusler Based SGSs

Half-Heusler (HH) alloys with XYZ chemical formula crystallize in the cubic C1b structure. Ternary Heusler compounds belonging to F-43m space group, have

1:1:1 composition, and fcc sublattice with three out of four positions occupied [46]. The HH alloys consist of two TM elements and one sp-element in their unit cell. The order of atomic positions based on the most energetically stable HH compounds is X at 4a (0,0,0), Y at 4c (¼, ¼, ¼) and Z at 4d (¾, ¾, ¾) Wyckoff positions [54]. Like other Heusler compounds, the HH alloys also obey the Slater-Pauling rule, M=Nv-18. In the minority band, there are 9 fully occupied bands; an s band and three p bands arising from sp-element and five d bands due to a TM atom. Hybridization between d orbitals of X and Y is responsible for the band gap in HH alloys [54].

In 2019, Zhang *et. al.* found via first principles calculations that FeMnGa exhibits SGS properties [69]. As being a HH alloy, hybridization between d-orbitals of Fe(X) and Mn(Y) atoms creates a bandgap in the minority spin channel. Antiparallel magnetic alignment between Fe and Mn atoms makes net magnetic moment zero with keeping fully spin-polarized current. Thus, FeMnGa is a fully compensated ferrimagnetic SGS. In Fig. 2.4, prototype of half-Heusler alloys is shown [48–50].

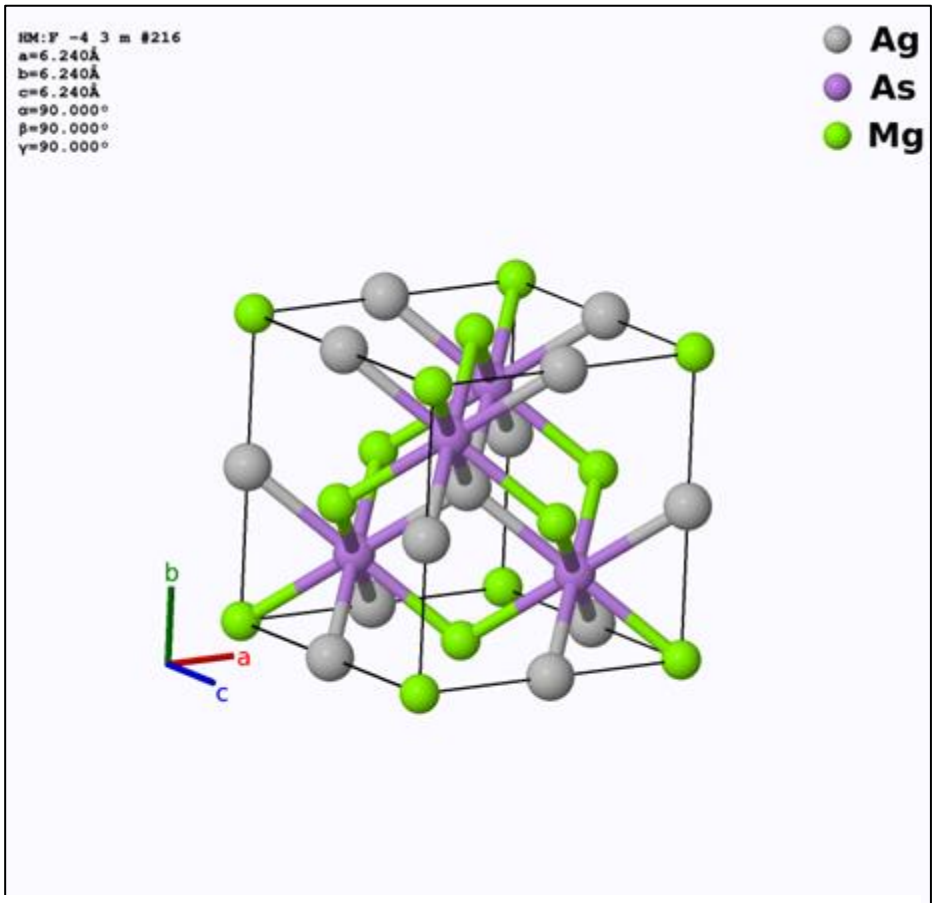

Figure 2.4: Prototype of half-Heusler

2.2 Dirac SGSs

A material with linear energy-momentum dispersion is known as Dirac material. Its linearly dispersed bands around the Fermi level imply that effective mass of charge carriers in the material can be eliminated [70]. Massless charge carriers, or Dirac fermions, provide almost no energy dissipation for materials. In 2016, Xiao-Lin Wang introduced spin-gapless materials that have linear dispersion around the Fermi level and fully spin polarization in their band structures [71]. As in the case for PSGSs, the Dirac SGSs (DSGSs) can be categorized according to spin-polarized behaviour of linearly dispersed conduction bands and valence bands at the Fermi energy level [33].

Type-I: In one spin channel a Dirac point is formed due to touching bottom of the CB and top of the VB to each other at E_F. On the other hand, the Fermi energy is located in between the valence and conduction bands in the other spin channel (Figure *2.5*a).

Type-II: Both spin channels have a gap, but the VB top in spin-up channel touches the CB bottom in the spin-down channel at Fermi energy (Figure *2.5*b).

Type-III: Gapless spin-up channel is responsible for Dirac states. The CB of two channels touch the Fermi level. Also, there is a gap between the valence and conduction bands in the spin-down channel (Figure *2.5*c).

Type-IV: There is no gap in the spin-up channel. However, the spin-down channel has a gap, and top of the VB touches the Fermi energy (Figure *2.5*d).

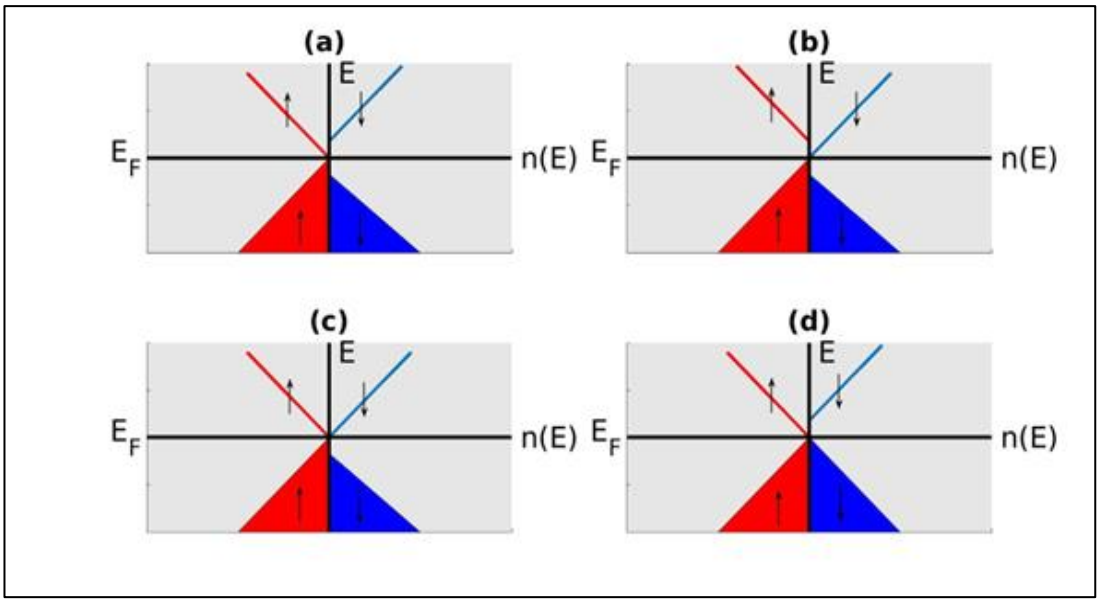

Figure 2.5: The Dirac SGSs

Dirac SGSs can be classified under two groups with respect to the orbital type that causes the Dirac state: p-state DSGS and d-state DSGS [60,72]. Since our focus is mainly the investigation of SGSs with parabolic dispersion relation, p-state DSGS and d-state DSGS will be briefly discussed by sample materials defined as DSGSs.

2.2.1 p-state DSGS

S. Davatolhagh and A Dehghan showed that CoKSb, a prototype d^0 - d HH alloy, exhibits not only linearly dispersed bands around the Fermi level, but also shows SGS behaviour [73]. In the d^0 - d HH compounds, d^0 is an alkali or alkaline-earth metal, and d is an TM [73–75]. Atomic positions in the unit cell of most energetically stable configuration are such that the TM element is located between the main group element and the alkaline-earth or alkali metal, and thus, d and d^0 atoms are the nearest neighbours [73]. Also, the sp-atom is the nearest and the next nearest neighbour of the TM atom and d^0 atom, respectively. Theoretical calculations done on CoKSb show that there is a Dirac node at the Fermi level in the majority spin channel [73,74]. The minority spin channel in the band structure of CoKSb has a band gap in between the valence and conduction bands with parabolic dispersions [73]. These unique properties in its band structure are indication for CoKSb being a DSGS. Being a HH, it follows the Slater-Pauling rule $M_t=18-N_v$, such that its total magnetic moment per unit cell is

3. In the majority spin channel, the Dirac state at the Fermi level arises from meeting of one p-orbital in the conduction band with one of the p-orbitals in the valence band at the gamma point, which make CoKSb a p-state Dirac SGS [73].

2.2.2 d-state DSGS

The TM trihalides with chemical formula TMX_3 have been investigated in the Dirac-like SGS search [72]. TMX_3 monolayers have rhombohedral crystal structure with prototype BiI_3 under the R3 space group [76]. In general, TMs forming 2D TMX_3 monolayers are V, Cr, Mn, Fe, Co, Ni, and Ru [33,77].

In 2016, He *et. al.* showed, via the first-principles calculations, both VCl_3 and VI_3 display linear dispersion and spin polarization [78]. In the layers of VCl_3 and VI_3, a honeycomb lattice is formed by centring vanadium atoms [60,76]. According to the results found by He *et. al.*, d orbitals of V atoms split into two-fold and three-fold degenerate orbitals with respect to octahedral crystal field are responsible for Dirac states [78]. Their calculated Curie temperatures are far below the room temperature, also their Dirac points are located above the Fermi energy [33,72,78]. To obtain the most stable magnetic configuration and to transform them from half-metallic phase to SGS phase, their Curie temperatures were increased by doping method [33,72,78]. As a result of electron doping, VCl_3 and VI_3 became DSGSs with $M_t = 4$ per unit cell. Fig 2.6 demonstrates the prototype of TMX_3 [48–50].

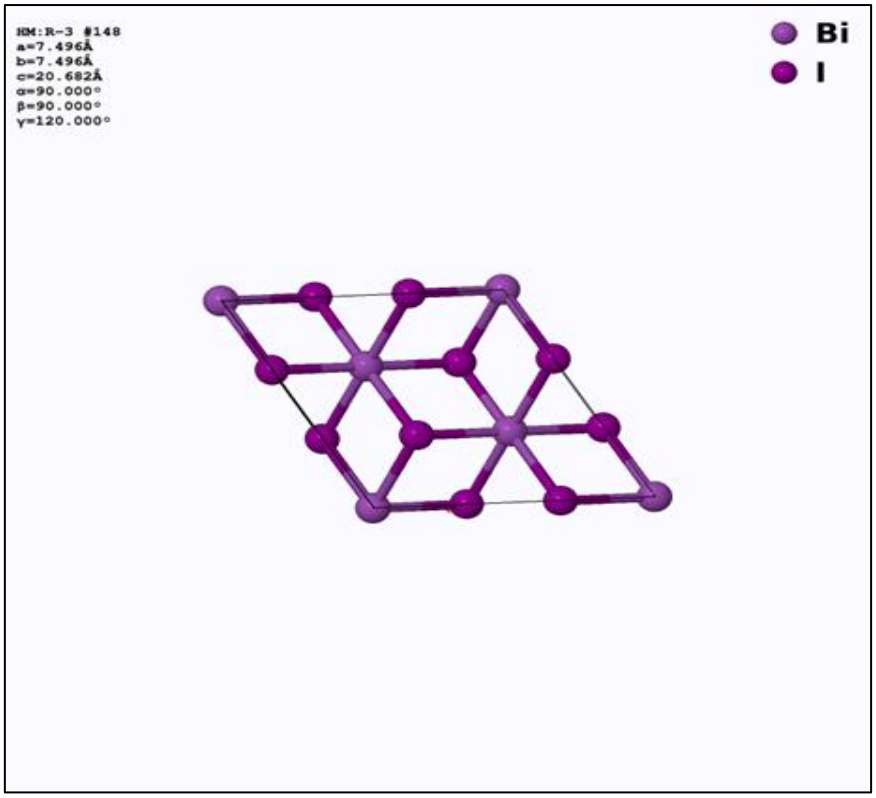

Figure 2.6: Prototype for TMX3.

3 METHODOLOGY

First-principles calculation is a method based on quantum mechanical laws to describe the physical properties of matter [79,80]. For instance, electrical and structural properties of materials can be modelled by specifying only atomic numbers and positions of atoms in the unit cell via first-principles calculations. For analysing electronic structure of solids, many-body problem in the basis of quantum mechanics must be established [81]. The Hamiltonian of solids contains the kinetic energies of electrons and nuclei, the electron-electron interaction, the inter nuclei interactions and the interactions between electrons and nuclei [82]. Finding the exact solution of many-body Schrödinger equation is certainly not the most efficient way to investigate solids, since the problem is too complicated to solve.

Taking into account Born-Oppenheimer approximation, Hamiltonian of the system is reduced to the electronic Hamiltonian [82,83],

$$\hat{H} = -\frac{1}{2}\sum_{i}^{N}\vec{\nabla}^2 + \frac{1}{2}\sum_{i}^{N}\sum_{j\,i\neq j}^{N}\frac{1}{|\vec{r}_i - \vec{r}_j|} - \sum_{i}^{N}\sum_{k}^{N}\frac{Z_k}{|\vec{r}_i - \vec{R}_k|} \tag{3.1}$$

or

$$\hat{H} = \sum_{i}^{N}\left(-\frac{\vec{\nabla}^2}{2} + v_{ext}(\vec{r}_i)\right) + \frac{1}{2}\sum_{\substack{i,j \\ i\neq j}}^{N}\frac{1}{|\vec{r}_i - \vec{r}_j|} \tag{3.2}$$

where the first sum term in the right-hand side is the kinetic energy of electrons plus any external potential, and the second one is the total electron-electron interaction potential energy. Further simplification can be achieved by assuming the electrons as independent of each other, and hence, writing down the wavefunction of the system as a product of one-electron orbitals [84]. In 1930, Vladimir Fock [85] ameliorated this

$$\Psi^{HF}(\vec{r}_1,\sigma_1,\vec{r}_2,\sigma_2,\ldots,\vec{r}_N,\sigma_N) = \frac{1}{\sqrt{N!}}det\begin{bmatrix}\varphi_i(\vec{r}_1,\sigma_1) & \cdots & \varphi_i(\vec{r}_N,\sigma_N)\\ \vdots & \ddots & \vdots \\ \varphi_N(\vec{r}_1,\sigma_1) & \cdots & \varphi_N(\vec{r}_N,\sigma_N)\end{bmatrix}. \tag{3.3}$$

Hartree approximation by replacing the wavefunction as a product of orbitals with forming the many electron wavefunction as a single Slater determinant,

The Hartree-Fock approximation states that Ψ^{HF} is the wavefunction which minimizes total energy of the system [79,85,86],

$$E^{HF} = \left\langle \Psi^{HF} \middle| \hat{H} \middle| \Psi^{HF} \right\rangle \qquad 3.4$$

Eq. *3.4* can be expressed as integral form,

$$E^{HF} = \int \varphi_i^*(\vec{r}) \left(-\frac{\vec{\nabla}^2}{2} + v_{ext}(\vec{r}_i) \right) \varphi_i(\vec{r}) d\vec{r} + \frac{1}{2} \sum_{i \neq j}^{N} \int \frac{\varphi_i^*(\vec{r}) \varphi_i(\vec{r}) \varphi_j^*(\vec{r\prime}) \varphi_j(\vec{r\prime})}{|\vec{r} - \vec{r\prime}|} d\vec{r} d\vec{r'} - \frac{1}{2} \sum_{i \neq j}^{N} \int \frac{\varphi_i^*(\vec{r}) \varphi_j(\vec{r}) \varphi_j^*(\vec{r\prime}) \varphi_i(\vec{r\prime})}{|\vec{r} - \vec{r\prime}|} d\vec{r} d\vec{r'} \qquad 3.5$$

or

$$E^{HF} = \sum_i^N \left\langle \varphi_i \middle| -\frac{\vec{\nabla}^2}{2} + v_{ext}(\vec{r}_i) \middle| \varphi_i \right\rangle + \frac{1}{2} \sum_{i \neq j}^{N} \left\langle \varphi_i \varphi_j \middle| \frac{1}{|\vec{r} - \vec{r\prime}|} \middle| \varphi_i \varphi_j \right\rangle - \frac{1}{2} \sum_{i \neq j}^{N} \left\langle \varphi_i \varphi_j \middle| \frac{1}{|\vec{r} - \vec{r\prime}|} \middle| \varphi_j \varphi_i \right\rangle .[79,85-87] \qquad 3.6$$

$$\left[-\frac{\vec{\nabla}^2}{2}+v_{ext}(\vec{r})+\sum_j^N\left\langle\varphi_j(\overrightarrow{r'})\left|\frac{1}{\left|\vec{r}-\overrightarrow{r'}\right|}\right|\varphi_j(\overrightarrow{r'})\right\rangle\right]\varphi_i(\vec{r}) \quad 3.7$$
$$-\sum_j^N\left\langle\varphi_j(\overrightarrow{r'})\left|\frac{1}{\left|\vec{r}-\overrightarrow{r'}\right|}\right|\varphi_i(\overrightarrow{r'})\right\rangle\varphi_j(\vec{r})=\varepsilon_i\varphi_i(\vec{r})$$

$$\left[-\frac{\vec{\nabla}^2}{2}+v_{ext}(\vec{r})+\int\frac{n(\overrightarrow{r'})}{\left|\vec{r}-\overrightarrow{r'}\right|}\right]\varphi_i(\vec{r})-\sum_j\int\frac{\varphi_j^*(\overrightarrow{r'})\varphi_j(\vec{r})}{\left|\vec{r}-\overrightarrow{r'}\right|}\varphi_i\left(\overrightarrow{r'}\right)=\varepsilon_i\varphi_i(\vec{r}) \quad 3.8$$

Then by using the variational approach, one-particle Hartree-Fock equations are obtained as [79,87,88]

In Eqs. *3.7* and *3.8*, third term on the left-hand side represents the Hartree potential, while the last term is known as the exchange interaction. In the Hartree-Fock approximation, the main assumption is that each electron is independent and interacts with a cluster of all other electrons [88]. The average potential includes non-local exchange potential and the Hartree, or Coulomb, potential [88]. This method enables the simplification of many-body system or many-electron problem to many single electronic systems. In other words, N-body problem is simplified to N times one-body problem with the mean-field external potential [87]. Although the reduced problem is much less complicated than the original one, the single electronic Schrödinger equation still needs to be solved N times, the number of electron orbitals in the system.

3.1 Density Functional Theory

Density functional theory (DFT) is an approach under the first-principles calculation method that analyse the physical properties of systems using the electron density instead of their wave function [89]. According to the Thomas-Fermi approximation, ground state energy of an electron system can be expressed as a functional of electronic density [89,90]. This provides a one-to-one mapping between the external potential and density [91]. In other words, starting from an external potential one can compute the ground state wave function and corresponding electron density self-consistently. DFT is based upon theorems developed by Nobel laurates

Pierre C. Hohenberg and Walter Kohn in 1964 [92]. In the first Hohenberg-Kohn theorem, it is shown that the one-to-one mapping, the statement of Thomas-Fermi model, is invertible [83,92]. To determine the external potential of an electronic system, it is sufficient to know the ground state electron density of the system. Hence, the ground state wave function and corresponding energy of the system can be computed with the information of the ground state electronic density. The central point of the first theorem is that operators acting on the system are functionals of the ground state electron density, and they are uniquely determined by that density [83,92]. The second Hohenberg-Kohn theorem states that electron density minimizing the total energy of the system is the exact ground state electron density of the real system [83,91,92]. We can express this statement mathematically as

$$E[\rho(\vec{r})] = \min_{\Psi\to\rho}\langle\Psi|\hat{H}|\Psi\rangle \tag{3.9}$$

These theorems enable us to establish the ground state properties of an interacting inhomogenous electronic system. Recalling Eq. *3.2*, Hamiltonian of the electronic system is

$$\hat{H} = \hat{T} + \hat{V}_{ext} + \hat{V}_{e-e}, \tag{3.10}$$

and total energy of the system is a functional of electronic density

$$E[\rho(\vec{r})] = T[\rho(\vec{r})] + V_{ext}[\rho(\vec{r})] + V_{e-e}[\rho(\vec{r})]. \tag{3.11}$$

The ground state energy can be computed by the variational theorem as [83]

$$E_0 = \min_{\rho}\left(\min_{\Psi}\langle\Psi|\hat{H}|\Psi\rangle\right). \tag{3.12}$$

External potential in the Hamiltonian depends only on the density. Thus the ground state energy expression can be separated as [83,92]

$$E_0 = \min_{\rho}\left(\min_{\Psi}\langle\Psi|\hat{T} + \hat{V}_{e-e}|\Psi\rangle + \int v(\vec{r})\rho(\vec{r})d\vec{r}\right) . \qquad 3.13$$

The first term in the right-hand side of Eq. 3.13 is named as the universal density functional and it is independent of the external potential acting on electrons in the system [93,94],

$$\begin{aligned} F[\rho(\vec{r})] &= \min_{\Psi}\langle\Psi|\hat{T} + \hat{V}_{e-e}|\Psi\rangle , \\ F[\rho(\vec{r})] &= \min_{\Psi}\langle\Psi|\hat{T} + \hat{V}_{e-e}|\Psi\rangle , \\ \therefore\ \hat{F}[\rho(\vec{r})] &= \hat{T}[\rho(\vec{r})] + \hat{V}_{e-e}[\rho(\vec{r})] . \end{aligned} \qquad 3.14$$

Then, the exact ground state energy of the system becomes [95],

$$E_0 = \min_{\rho}(F[\rho(\vec{r})] + \int v(\vec{r})\rho(\vec{r})d\vec{r}) \ . \qquad 3.15$$

In Eq. 3.14, the universal functional is decomposed into kinetic energy and potential energy parts in the basis of real interacting system. The problem is to approximate the universal functional, $F[\rho(\vec{r})]$.

In 1965, Walter Kohn and Lu Sham came up with the idea of mapping interacting many-body electronic system onto a non-interacting electronic system [96]. Namely, they mapped a real system onto a fictitious system of N non-interacting electrons which is defined in terms of N single-particle orbitals [83,95]. In such a system Schrödinger equation of the single-particle orbitals is constructed; and single-particle ground state density is expressed as a set of single-particle orbitals [89,95],

$$\left(-\frac{1}{2}\vec{\nabla}^2 + v_{eff}\right)\phi_i = \varepsilon_i\phi_i\,. \tag{3.16}$$

$$\rho_{sp}(\vec{r}) = \sum_i^N |\phi_i(\vec{r})|^2 \tag{3.17}$$

The energy functional of the Kohn-Sham system is,

$$E_{sp}[\rho_{sp}] = T_{sp}[\rho_{sp}] + V_{eff}[\rho_{sp}]. \tag{3.18}$$

Convenience of the Kohn-Sham model is that single-particle ground state electron density minimizing total energy of the Kohn-Sham system is equal to the electron density of the real system in its ground state [89,96], that is

$$\rho_{sp}(\vec{r}) = \rho(\vec{r}). \tag{3.19}$$

From this point of view, Kohn and Sham decomposed the universal functional $F[\rho(\vec{r})]$ into three terms: kinetic energy of a system of non-interacting electrons, the Hartree energy and the exchange-correlation energy functionals,

$$F[\rho] = T_{sp}[\rho] + V_H[\rho] + E_{xc}[\rho], \tag{3.20}$$

and total energy functional,

$$E[\rho] = F[\rho] + V_{ext}[\rho], \tag{3.21}$$

$$E[\rho] = T_{sp}[\rho] + V_H[\rho] + E_{xc}[\rho] + V_{ext}[\rho] \tag{3.22}$$

Where $V_H[\rho] = \frac{1}{2}\iint \frac{\rho(\vec{r})\rho(\overrightarrow{r'})}{|\vec{r}-\overrightarrow{r'}|} d\vec{r}d\overrightarrow{r'}$, and $V_{ext}[\rho] = \int \rho(\vec{r})v(\vec{r})d\vec{r}$ [89,95]. Thus, for an effective potential associated with electron density of the non-interacting system, which is equal to the ground state electron density of the real interacting many-

$$E[\rho] = T_{sp}[\rho] + \frac{1}{2}\iint \frac{\rho(\vec{r})\rho(\overrightarrow{r'})}{\left|\vec{r}-\overrightarrow{r'}\right|} d\vec{r}d\overrightarrow{r'} + \int \rho(\vec{r})v(\vec{r})d\vec{r} + E_{xc}[\rho]. \tag{3.23}$$

body system, the total energy functional can be described as,

When a small enough variation is applied to the ground state electron density, the energy functional in Eq. 3.18 becomes stationary [89,97]

$$\delta E_{sp} = \delta(T_{sp}[\rho] + V_{eff}[\rho]) \tag{3.24}$$

$$0 = \delta(T_{sp}[\rho] + \int v_{eff}(\vec{r})\rho(\vec{r})d\vec{r}) \tag{3.25}$$

$$\Rightarrow \delta T_{sp} = -\int v_{eff}(\vec{r})\rho(\vec{r})d\vec{r} \tag{3.26}$$

Similarly, for Eq. *3.23*,

$$0 = \delta T_{sp}[\rho] + \int \rho(\vec{r})d\overrightarrow{r} \left[\frac{\rho(\overrightarrow{r'})}{\left|\vec{r}-\overrightarrow{r'}\right|} d\overrightarrow{r'} + v(\vec{r}) + \frac{\delta E_{xc}[\rho]}{\delta\rho(\vec{r})}\right], \tag{3.27}$$

and using Eq. *3.26* [98],

$$v_{eff}(\vec{r}) = v_H(\vec{r}) + v(\vec{r}) + v_{xc}(\vec{r}), \qquad 3.28$$

Where $v_{xc}(\vec{r}) = \frac{\delta E_{xc}[\rho]}{\delta \rho(\vec{r})}$.

Total energy functional for the real system, equation *3.23*, is divided into single particle kinetic energy, the external potential energy, the Hartree energy and the exchange-correlation energy functionals. The last term of the right-hand side in equation *3.23* includes corrections coming from the kinetic energy of interacting electrons and correlations due to the Coulomb interaction [89]. The exchange-correlation energy functional decomposes into the exchange functional $E_x[\rho]$, and the correlation energy functional, $E_c[\rho]$ [95]. Apart from $E_{xc}[\rho]$, other terms in Eq. *3.23* can be computed numerically. Kohn-Sham DFT focuses on approximate calculations of the exchange-correlation energy functional.

For spin-polarized systems, where the numbers of spin-up and spin-down electrons are unequal, Hamiltonian including the effective potential and charge density become spin-dependent. Thus, exchange and correlation functional and basis functions for the spin-polarized system also convert into spin-dependent quantities [98].

In the Kohn-Sham DFT, the method for dealing with a real system is to map the real system onto the non-interacting single electron problem. By solving single-particle Schrodinger equation, one-particle electron density and corresponding external potential acting on the system are found. The Kohn-Sham electron density which minimizes total energy functional is the correct ground state electron density of the real interacting many-body problem. Thus, once the ground state $\rho(\vec{r})$ is known, then all quantities such as ground state energy, external potential and ground state wavefunctions etc. of the system can be obtained. As it is mentioned earlier, approximations are made on the exchange and correlation term. The closeness of results calculated with DFT to the experimental ones depends on the choice of the approximation level [99]. The semi-local approximation methods used in DF are listed in Table 3.1 [83,99].

Table 3.1 The semi-local approximation methods used in DFT.

$LDA\colon\ \rho\ \longrightarrow E_{xc}^{LDA}[\rho] = \int \rho(\vec{r})\, \varepsilon_{xc}^{UEG}\big(\rho(\vec{r})\big) d\vec{r}$
$GGA\colon\ \rho\ , \left\vert\vec{\nabla}\rho\right\vert\ \rightarrow E_{xc}^{GGA}[\rho] = \int e_{xc}^{GGA}\left(\rho(\vec{r}), \vec{\nabla}\rho(\vec{r})\right) d\vec{r}$
$Meta-GGA\colon \rho\ , \left\vert\vec{\nabla}\rho\right\vert, \tau\ \rightarrow E_{xc}^{m-GGA}[\rho,\tau] = \int e_{xc}^{m-GGA}\left(\rho(\vec{r}), \vec{\nabla}\rho(\vec{r}), \nabla^2\rho, \tau(\vec{r})\right) d\vec{r}$ $\tau(\vec{r}) = \frac{1}{2}\sum_i^N \vert\nabla\phi_i(\vec{r})\vert$

Local-density approximation (LDA) is the simplest approach in which the exchange-correlation energy density of uniform electron gas depends only on the density at a particular point [91,95]. Generalized gradient approximation (GGA) depends on the density and its gradient at every point [95]. Meta-GGA is also considered as a semi-local approximation and uses kinetic energy density of the Kohn-Sham system as well as electron density and its gradient [99]. As there is no any systematic approach, each semi-local approximation has its own pros and cons.

In summary, DFT on the basis of the Hohenberg-Kohn theorems and Kohn-Sham Scheme focuses only on the ground state features of many-body problem such as crystalline solids. Also, it is important to note that since the Kohn-Sham system is a hypothetical system, the Kohn-Sham wavefunctions and corresponding eigenvalues have no any physical meaning. DFT is one of the most preferred first-principles calculation method, since it provides significant simplification over computing real systems i.e., solids. Yet, it has limitations in some manners such as in bandgap values, self-interaction errors and not valid for excited states.

3.2 The *GW* Approximation

Behaviour of the valence and conduction bands around the Fermi energy is crucial in material classification. Calculations done for a material in its ground state may overestimate or underestimate its bandgap energy. Thus, the problem at hand is extended to include the excited states of the system. In 1965, Lars Hedin proposed the *GW* approximation based on many-body perturbation theory [100] .

Green functions used for solving inhomogeneous differential equations with specified boundary conditions provide physical interpretations for excitation states of

many-body systems. In this sense, Green's function can be thought as a propagation operator, or shortly propagator, associated with addition or removal of a particle in the N-electron system at its ground state [101]. By definition, single particle Green's function (with h=1) is,

$$iG(\vec{r},t;\vec{r}',t') = \langle \Psi_0^N | \hat{T}[\hat{\psi}(\vec{r},t), \hat{\psi}^+(\vec{r}',t')] | \Psi_0^N \rangle. \quad 3.29$$

It gives the probability amplitude for propagating an additional particle created at $(\vec{r}',t')$, from $(\vec{r}',t')$ to $(\vec{r},t)$ in a N-electron system [102]. In Eq. *3.29*, Ψ_0^N is the N-electron ground state wavefunction, $\hat{\psi}^+$ is the creation operator of one particle at the position $\vec{r}'$ and time t', and the annihilation operator $\hat{\psi}$ is responsible for removing of a particle at position $\vec{r}$ and a later time t > t'. To clarify the relation between time-ordered single particle Green's funtion and excitation states of the N-particle system, one can rewrite Eq. *3.29* with Schrödinger representation [103,104],

$$G(\vec{r},t;\vec{r}',t') = -i\sum_i \langle \Psi_0^N | \hat{\psi}(\vec{r}) e^{-iHt} | \Psi_i^{N+1} \rangle \langle \Psi_i^{N+1} | \hat{\psi}^+(\vec{r}') e^{iHt'} | \Psi_0^N \rangle$$
$$- i\sum_i \langle \Psi_0^N | \hat{\psi}^+(\vec{r}') e^{iHt'} | \Psi_i^{N-1} \rangle \langle \Psi_i^{N-1} | \hat{\psi}(\vec{r}) e^{-iHt} | \Psi_0^N \rangle. \quad 3.30$$

Then it becomes

$$iG(\vec{r},t;\vec{r}',t') =$$
$$\Theta(t-t')\sum_i \langle \Psi_0^N | \hat{\psi}(\vec{r}) | \Psi_i^{N+1} \rangle \langle \Psi_i^{N+1} | \hat{\psi}^+(\vec{r'}) | \Psi_0^N \rangle e^{-i(E_i^{N+1}-E_0^N)(t-t')} -$$
$$\Theta(t-t')\sum_i \langle \Psi_0^N | \hat{\psi}^+(\vec{r}') | \Psi_i^{N-1} \rangle \langle \Psi_i^{N-1} | \hat{\psi}(\vec{r}) | \Psi_0^N \rangle e^{-i(E_0^N-E_i^{N-1})(t-t')} \quad 3.31$$

or

$$iG(\vec{r},t;\vec{r}',t') = \Theta(t-t')\sum_i \varphi_i^{N+1}(\vec{r})\,\varphi_i^{N+1*}(\vec{r}')e^{-i\varepsilon_i^{N+1}(t-t')} - \Theta(t-t')\sum_i \varphi_i^{N-1*}(\vec{r}')\,\varphi_i^{N-1}(\vec{r})e^{-i\varepsilon_i^{N+1}(t-t')}, \quad 3.32$$

where $\varphi_i^{N\pm1}(\vec{r})$ is known as the Lehmann amplitüde, and $\varepsilon_i^{N\pm1}$ represents excited eigenvalues [103,104]. Eqs. 3.29 - 3.32 demonstrate that excitation states and their energies can be indicated and analysed in the basis of one-particle Green's function. However, as it is clearly seen in Eq. *3.29*, projected wavefunctions are the ground state many-body wavefunctions. One of the starting point of the *GW* approximation is to calculate the one-particle Green's function without dealing with many-body wavefunction. The equation of motion for the one-particle Green's function is Eq. 3.33 [105].

$$i\frac{\partial}{\partial t}G(\vec{r},t;\vec{r}',t') = \delta(\vec{r}-\vec{r}')\delta(t-t') + h_0(\vec{r})G(\vec{r},t;\vec{r}',t') - i\int d\vec{r}"\, v(\vec{r},\vec{r}")G(\vec{r}t,\vec{r}",t;\vec{r}'t',\vec{r}",t^+). \quad 3.33$$

In this relation, second term on the right-hand side is non-interacting quantity, and the last term is perturbing or interacting term. In quantum mechanical perturbation theory, interactions (or perturbations) are given in terms of scattering potential.

$$\left[i\frac{\partial}{\partial t} - h_0(\vec{r})\right] G(\vec{r},t;\vec{r}',t') = \delta(\vec{x},\vec{x}') - i\int d\vec{r}"\, v(\vec{r},\vec{r}")G(\vec{r}t,\vec{r}",t;\vec{r}'t',\vec{r}",t^+), \quad 3.34$$

$$\delta(\vec{x},\vec{x}') = \delta(\vec{r}-\vec{r}')\delta(t-t'). \quad 3.35$$

So as to determine the one-particle Green's function, two-particle Green's function should be known. Complexity of the problem continues to accelerate i.e.,

$$G_1 \leftarrow G_2\ ;$$
$$G_1 \leftarrow G_2 \leftarrow G_3\ ;$$
$$G_1 \leftarrow G_2 \leftarrow G_3 \leftarrow G_4 \ldots$$

Instead of solving Eq. 3.34 with the Green's function in ascending many-body theory, an effective potential that includes all interactions and excitations associated with the system is introduced, like in Eq. 3.36 [106,107]

$$\left[i\frac{\partial}{\partial t} - h_0(\vec{r}) - V_H(\vec{r})\right] G(\vec{r},t;\vec{r}',t') = \delta(\vec{x},\vec{x}') + \int d\vec{r}"\, \Sigma(\vec{r},t;\vec{r}",t) G(\vec{r},t;\vec{r}",t). \quad 3.36$$

In the case of non-interacting systems, integral on the right-hand side gives zero, and we simply have

$$\left[i\frac{\partial}{\partial t} - h_0(\vec{r}) - V_H(\vec{r})\right] G_0(\vec{r},t;\vec{r}',t') = \delta(\vec{x},\vec{x}'). \quad 3.37$$

Since the focus is the term consisting of excitations and corrections, one can make Fourier transformation to formulate Eq. 3.36 in the frequency domain [103,106,107]

$$[w - h_0(\vec{r}) - V_H(\vec{r})]\, G(\vec{r},\vec{r}';w) = \int d\vec{r}"\, \Sigma(\vec{r},\vec{r}";w) G(\vec{r}",\vec{r}';w). \quad 3.38$$

One-particle Green's function for the interacting many-particle system can be obtained by using Eqs. 3.36 and 3.38, known as the Dyson equation [103,107,108],

$$G = G_0 + G_0 \Sigma G, \\ = G_0 + G_0 \Sigma G_0 + G_0 \Sigma G_0 \Sigma \mathrm{G} + \cdots \quad 3.39$$

The Dyson equation is an expression for time-ordered one-particle Green's function in terms of an infinite series of non-interacting Green's function G_0, and electronic self-energy, or scattering potential, Σ.

In the *GW* method, approximations made to obtain the Green's funtion are for the self-energy [103]. For further analysis, Fourier transformation is applied to one-particle Green's funtion (Eq. 3.32), then plugged in the equation of motion for Green's funtion in the frequency domain (Eq. 3.38) [103,106],

$$\sum_i \frac{\varphi_i^{*N\pm1}(\vec{r}')}{w - \varepsilon_i^{N\pm1} \pm i\eta} \{[w - h_0(\vec{r}) - V_H(\vec{r})]\varphi_i^{N\pm1}(\vec{r}) \\ - \int d\vec{r}" \, \Sigma(\vec{r}, \vec{r}"; w)\varphi_i^{N\pm1}(\vec{r}')\} = \delta(\vec{r}, \vec{r}'). \quad 3.40$$

After Eq. 3.40 is multiplied by $w - \varepsilon_i^{N\pm1}$, and taking the limit $w \to \varepsilon_i$, the equation of motion becomes

$$[h_0(\vec{r}) - V_H(\vec{r})]\varphi_i^{N\pm1}(\vec{r}) - \int d\vec{r}" \, \Sigma(\vec{r}, \vec{r}"; \varepsilon_i)\varphi_i^{N\pm1}(\vec{r}') = \varepsilon_i^{N\pm1}\varphi_i^{N\pm1}(\vec{r}). \quad 3.41$$

The self-energy $\Sigma(\vec{r}, \vec{r}"; \varepsilon_i)$ contains all corrections in the many-body system. To approximate the effective potential term in Eq. 3.41, the approach is to consider the interacting system in the perspective of a quasiparticle picture [79,103]. A quasiparticle is composed of an electron or a hole with its Coulomb screening cloud. If an electron is removed from the system of N-particle ground state, a positively charged hole is created due to the electron removal. Then, arises Coulomb interaction between the positively screened charge and electrons. Excited electrons start moving towards the screened charge; thus, for each electron in the system there exists a hole where the electrons initially occupied. This implies that a polarization is induced due to electron-hole pairs in the response of an additional positive charge (hole). The screened potential due to a quasiparticle embraces Coulomb interaction caused by the central particle (electron or hole) and all the interactions related to the screening cloud

[102]. In fact, screened Coulomb potential can be expressed in the form of a geometric series as in the Green's function,

$$W = v + vPv + vPvPv + vPvPvPv + \cdots \quad 3.42$$

$$\Rightarrow W = v + vPW, \quad 3.43$$

or in the integral form [109,110],

$$W(\vec{r},\vec{r}';w) = \mathrm{v}(\vec{r},\vec{r}') + \int d\vec{r}'''d\vec{r}''\,\mathrm{v}(\vec{r},\vec{r}'')\mathrm{P}(\vec{r}'',\vec{r}''';w)W(\vec{r}''',\vec{r}';w). \quad 3.44$$

The screening polarization can be calculated though the random-phase approximation (RPA) proposed by D. Bohm and D. Pines [111]. The RPA polarization function comprises the non-interacting electron-hole pairs [110,112]. Hence, the screening polarization function in the frequency domain becomes,

$$P(\vec{r},\vec{r}';w) = -iG_0(\vec{r},\vec{r}';w)G_0(\vec{r}',\vec{r};w), \quad 3.45$$

where G_0 is the Green's function of the non-interacting system as in Eq. *3.37*. The self-energy is written in the time domain as [103,112],

$$\Sigma(\vec{r},t;\vec{r}',t') = iG(\vec{r},t;\vec{r}',t')W(\vec{r},t;\vec{r}',t'). \quad 3.46$$

The variation of correlational effects, $\frac{\partial\Sigma}{\partial G}$, is neglected, and the first interaction term in the self-energy expression is taken into account in the *GW* approximation. As a result, the self-energy becomes

$$\Sigma^{GWA}(\vec{r},t;\vec{r}',t') = iG_0(\vec{r},t;\vec{r}',t')W(\vec{r},t;\vec{r}',t'). \quad 3.47$$

Self-energy in the *GW* approximation contains the exchange and many-body correlation effects. It is non-local, non-hermitian and dynamical quantity. Hence, the *GW* approximation provides better results for an effective potential compared to the Hartree-Fock approximation and DFT.

3.3 Implementation and Details of Calculations

In the following we will discuss implementation of the DFT and *GW* approximation and details of our calculations.

3.3.1 Implementation of DFT

In our DFT calculations we used the free code FLEUR, which has been developed at Jülich research center, Germany. FLEUR employs the full-potential linearized augmented plane-wave method (FLAPW), which is an all-electron approach, in order to solve the Kohn-Sham problem [113]. On the contrary to pseudopotential method, all-electron approach prevents the Coulomb potential diverging as r approaches zero, and includes core electrons in the calculations as well as valence electrons. The FLAPW method enables the full-potential and charge density to be treated in the partitions of LAPW basis without any shape-approximation [114,115]. Wavefunctions corresponding to valence electrons are written in terms of the LAPW basis set [116].

In 1937, Slater introduced the augmented plane-wave (APW) method which divides the unit cell into regions: the muffin-tin (MT) spheres surrounding each atom, and the interstitial region (IR) [117]. The APW basis functions consist of radial functions and spherical harmonics in the MT spheres, while in the IR they are plane waves. These functions must be continuous on the surface of the MT. It is known that the APW basis has some problems. For instance, in order to define the Kohn-Sham wavefunctions in terms of the APW basis set, energy parameter must be set to the corresponding eigenvalue [95]. This results in non-linearity in the eigenvalue problem. In addition, vanishing radial function on the boundaries of the spheres makes coefficients in the MT region to have asymptotic behaviour, which leads to discontinuity [98]. Krogh Andersen obviated those problems by modifying the APW

basis set and transformed a non-linear problem into the linear one. In other words, Andersen linearized the APW basis set by extending radial functions to their first derivatives with respect to the energy parameter in the MT basis functions [118]. If Taylor series expansion is applied to the radial function around an arbitrary energy parameter i.e., E_l^i , the radial function becomes [95,98],

$$u_l^i(r_i,\epsilon)|_{E_l^i} = u_l^i\left(r_i,E_l^i\right) + \left(\epsilon - E_l^i\right)\dot{u}_l^i\left(r_i,E_l^i\right) + \left(\epsilon - E_l^i\right)^2\ddot{u}_l^i\left(r_i,E_l^i\right) + O\left(r_i,E_l^i\right). \quad 3.48$$

By taking expansion of radial function up to the linear order, the LAPW basis functions are expressed as [95,98],

$$\varphi_{\vec{k},\vec{G}}(\vec{r}) = \begin{cases} \frac{1}{\Omega}e^{i(\vec{k}+\vec{G})\cdot\vec{r}}, & \vec{r}\in IR \\ \sum_{l,m}[A_{lm}^{i\vec{G}}(\vec{k})u_l^i(r_i,E_l^i) + B_{lm}^{i\vec{G}}(\vec{k})\dot{u}_l^i(r_i,E_l^i)]Y_{lm}(\hat{r}_i), & \vec{r}\in MT_i \end{cases}. \quad 3.49$$

Wavefunctions in the IR stay the same as in the APW basis. In the MT spheres, the radial function and its energy derivative are denoted at fixed energy parameter [118,119]. This indicates that the MT basis functions become energy-independent [95,118]. Thus, the non-linear eigenvalue problem is reduced to the linear one. Furthermore, writing MT wavefunctions as a linear combination of u_l^i and $\dot{u}_l^i$, removes the discontinuity thanks to coefficients $A_{lm}^{i\vec{G}}$ and $B_{lm}^{i\vec{G}}$ [95,98,115].

In the all-electron FLAPW method, core and valence electrons are treated separately to increase computational accuracy and efficiency. So as to make separate treatment, the wavefunctions of the core and valence electrons should be orthogonal to each other [118]. Effective potential that the FLAPW method takes into account during the core state calculations is spherical due to associated atomic nucleus for each core electron [115,120]. The closer the electrons are to the atomic nucleus, the more kinetic energy they have. As a result, core electron states are obtained through a fully relativistic treatment.

Energy levels of electrons in a crystal structure inform us about their quantum states. Core electrons are located at low energies, and thus they are highly localized in the MT of the associated atom. On the contrary, valence electrons whose energies are near the Fermi energy are delocalized. During calculations, making a distinction between valence and core electrons with considerably low energy values is usually quite easy. However, for same cases, in the unit cell there exist core states with relatively high energy such that they are almost delocalized like valence electrons [95,115,116,120]. Neglecting these types of electrons may cause incorrect energy band calculations. The FLAPW method enables electrons with energies in between core states and valence states, so-called semi-core electrons, to be treated as valence electrons optionally [115]. In such cases, the MT sphere wavefunctions in the LAPW basis are extended to include these semi-core states by local orbital extension [115,116,120]. Additional radial functions $u_l^i(r_i, E_l^{LO})$, which are also confined in the MT sphere, are introduced such that local orbitals in the extension of the LAPW basis are determined [95,98,116],

$$\varphi_{\vec{k},lm}^{i,LO}(\vec{r}) = \begin{cases} 0, & \vec{r} \in IR \\ \left[A_{lm}^{LO} u_l^i(r_i, E_l^i) + B_{lm}^{LO} \dot{u}_l^i(r_i, E_l^i) + C_{lm}^{LO} u_l^i(r_i, E_l^{i,LO})\right] Y_{lm}(\hat{r}_i), & \vec{r} \in MT_i \end{cases} \quad 3.50$$

The local orbitals obtained from a linear combination of radial functions and their derivatives in the LAPW basis and an additional radial function with energy $E_l^{i,LO}$,

$$u_l^{i,LO}(r_i) = A_{lm}^{LO} u_l^i(r_i, E_l^i) + B_{lm}^{LO} \dot{u}_l^i(r_i, E_l^i) + C_{lm}^{LO} u_l^i(r_i, E_l^{LO}) \quad 3.51$$

are localized in the MT sphere [95]. Naturally, they become zero on the MT boundary with the help of coefficients A_{lm}^{LO}, B_{lm}^{LO} and C_{lm}^{LO} in the equation [95,116]. In the

FLAPW method, a division of the unit cell into the regions implies regional dependent charge density and potential as well [115,116,121].

$$\rho(\vec{r}) = \begin{cases} \sum_{\vec{G}} \rho_{\vec{G}} e^{i\vec{G}\cdot\vec{r}}, & \vec{r} \in IR \\ \sum_{L} \rho_L^i(r_i) Y_L(\hat{r}_i), & \vec{r} \in MT_i \end{cases}. \qquad 3.52$$

Charge density partitioned into the IR and MT spheres is expressed in Eq. *3.52*. Similarly, the effective potential in the FLAPW method is [115,116,121],

$$V_{eff}(\vec{r}) = \begin{cases} \sum_{\vec{G}} V_{eff}^{\vec{G}} e^{i\vec{G}\cdot\vec{r}}, & \vec{r} \in IR \\ \sum_{L} V_{eff}^{L,i}(r_i) Y_L(\hat{r}_i), & \vec{r} \in MT_i \end{cases}. \qquad 3.53$$

In summary, the FLAPW method implemented by the FLEUR code provides different treatments for different regions in the unit cell, and takes all electrons into account. Thanks to the FLAPW method, FLEUR code offers an option for semi-core states to be treated as either valence or core states. Hence, describing the semi-core states as local orbitals in the FLEUR code, we prevent from getting ghost bands in the band structure calculations [115,116].

In the following, we will discuss how we determine the parameters that will determine the most relevant results in our computations. In the FLAPW basis used for the valence electrons, some parameters must be assigned to limit radial functions in the MT spheres and planewaves in the IR of the unit cell. The cutoff parameter for reciprocal plane wave, K_{max}, is defined to specify how many plane waves the basis set in the IR includes. In the MT region, maximum angular momentum l_{max} is the convergence parameter to restrict the summation in the MT sphere. As there is matching in between functions in the MT spheres and plane waves in the IR, the choice of cut-off parameters in both regions should be related to each other. For instance, setting angular momentum cutoff parameter for i-th MT sphere relies on the radius of the associated muffin-tin sphere and K_{max} [122,123];

$$l^i_{max} \approx K_{max} \cdot R^i_{MT}. \quad 3.54$$

The density and effective potential expressions in the IR have the reciprocal cutoff parameter G_{max} to limit linear combination of planewave expansion [122]. Furthermore, there is another cutoff parameter for the exchange-correlation potential in the reciprocal space G^{xc}_{max}. Determination of G_{max} and G^{xc}_{max} parameters is based on the relation of G_{max} and G^{xc}_{max} to K_{max} [122],

$$G_{max} \geq G^{xc}_{max} \geq 2 \cdot K_{max}\,, \quad 3.55$$

$$G_{max} \approx 3 \cdot K_{max} \quad and \quad G^{xc}_{max} \approx 2.5 \cdot K_{max}\,. \quad 3.55$$

3.3.2 Implementation of *GW*

For our *GW* calculations we used the free code SPEX, a family member of the Jülich FLAPW codes. It is based on the MBPT we discussed above in detail, and it uses the output data obtained from a DFT code as input [113]. In this sense, SPEX provides complementary results including the excited state calculations for materials.

In sections 3.1 and 3.2, we already mentioned the equations of motions of Kohn-Sham and quasiparticle models in the DFT and *GW* approximation. The equations

$$\hat{h}(\vec{r})\phi^{\sigma}_{\vec{k}i}(\vec{r}) + V^{\sigma}_{xc}(\vec{r})\phi^{\sigma}_{\vec{k}i}(\vec{r}') = \varepsilon^{\sigma}_{\vec{k}i}\phi^{\sigma}_{\vec{k}i}(\vec{r}) \quad \text{and,} \quad 3.56$$

$$\hat{h}(\vec{r})\psi^{\sigma}_{\vec{k}i}(\vec{r}) + \int d\vec{r}'\,\Sigma^{\sigma}\left(\vec{r},\vec{r}';E^{\sigma}_{\vec{k}i}\right)\psi^{\sigma}_{\vec{k}i}(\vec{r}') = E^{\sigma}_{\vec{k}i}\psi^{\sigma}_{\vec{k}i}(\vec{r}) \quad 3.57$$

are, respectively, the Kohn-Sham relation in DFT and the quasiparticle equation in *GW*, with spin σ. In the right-hand side of Eq. 3.57, $E^{\sigma}_{\vec{k}i}$'s are the excitation energies of real system. The *GW* approach enables us to express the excitation energies as a correction to Kohn-Sham eigenvalues [110]

$$E^{\sigma}_{\vec{k}i} = \varepsilon^{\sigma}_{\vec{k}i} + \left\langle \phi^{\sigma}_{\vec{k}i} \middle| \Sigma^{\sigma}\left(E^{\sigma}_{\vec{k}i}\right) - V^{\sigma}_{xc} \middle| \phi^{\sigma}_{\vec{k}i} \right\rangle. \quad 3.58$$

Obviously, Eq. 3.58 is a non-linear equation, and it is obtained from the first order perturbation theory [110]. In SPEX, the excitation energies are computed from both linear and non-linear quasiparticle equations.

For *GW* calculations, the required basis sets are the ones containing wavefunctions and another basis set to represent all the interactions denoted as a product of the wavefunctions [124]. As SPEX code uses the FLAPW method, the mixed product basis (MPB) is chosen to describe products of LAPW functions. To comprehend the need for product basis set in *GW*, one revisits the self-energy expressed by the screened interaction and single-particle Green's function in the basis of Kohn-Sham eigenfunctions. The self-energy is expressed as

$$\Sigma^{\sigma}(\vec{r},\vec{r}',w) = \frac{i}{2\pi}\int dw' e^{iw'\eta}\, G_0^{\sigma}(\vec{r},\vec{r}';w+w')\, W(\vec{r},\vec{r}';w'), \tag{3.59}$$

where $W(\vec{r},\vec{r}';w')$ is the effective Coulomb interaction, and $G_0^{\sigma}(\vec{r},\vec{r}';w)$ is the non-interacting Green's function for a given spin in the frequency domain [103,110,112]

$$G_0^{\sigma}(\vec{r},\vec{r}';w) = \sum_{\vec{k}}\sum_{i} \frac{\phi_{\vec{k}i}^{\sigma}(\vec{r})\,\phi_{\vec{k}i}^{\sigma *}(\vec{r}')}{w-\varepsilon_{\vec{k}i}^{\sigma}+i\eta\, sgn(\varepsilon_{\vec{k}i}^{\sigma})}. \tag{3.60}$$

When Eq. 3.60 is plugged into Eq. 3.43, the polarization function within the RPA contains the representation of product basis set. In general expressions for matrix form of quantities involving more than one particle such as their interactions within themselves and/or each other, a basis set consisting of wavefunction products is preferred [95,110,112]. The MPB uses separate function sets to describe the expansion of wave function products. On the basis of LAPW, each of the two sets, one of which is the product of the MT functions and the other of the IR wavefunctions, is defined only in the respective region [109]

$$u_{lp}^{\sigma i}(r)u_{l'p'}^{\sigma i}(r)Y_{lm}^{*}(\hat{r})Y_{l'm'}(\hat{r}) \qquad for\ MT \tag{3.61}$$

$$e^{i(\vec{k}+\vec{G})\cdot\vec{r}}e^{i(\vec{k}\prime+\vec{G}\prime)\cdot\vec{r}} \qquad for\ IR \tag{3.62}$$

In Eq. 3.61 the problem arises from the product of radial functions for being not orthonormal. After diagonalizing the overlap matrix using products of spin-dependent radial functions, orthonormal and spin-independent wavefunction products are obtained in the MT region.

$$M_{LMP}^{i}(\vec{r}) = M_{LM}^{i}(r)Y_{LM}(\hat{r}), \tag{3.63}$$

where $|l-l'| \le L \le l+l'$, $-L \le M \le L$ and index p represents the combinations of indices l, l', p and p' [95,110,124]. For the IR, products of planewaves generate another planewave

$$M_{\vec{k},\vec{G}}(\vec{r}) = \frac{1}{\sqrt{V}}e^{i(\vec{k}+\vec{G})\cdot\vec{r}}\Theta(\vec{r}), \tag{3.64}$$

where $\Theta(\vec{r})$ is the Heaviside step function [95,124]

$$\Theta(\vec{r}) = \begin{cases} 1, & \vec{r} \in IR \\ 0, & \vec{r} \in MT_i \end{cases}. \tag{3.65}$$

In the *GW* approximation, the self-energy is divided into exchange and correlation terms by indicating the screened interaction as a summation of the bare Coulomb potential and the correlation part [105,110].

$$\Sigma_c^{\sigma}(\vec{r},\vec{r}',w) = \frac{i}{2\pi}\int dw'\, G_0^{\sigma}(\vec{r},\vec{r}';w+w')W_c(\vec{r},\vec{r}';w'), \tag{3.66}$$

$$\Sigma_x^{\sigma}(\vec{r},\vec{r}') = \frac{i}{2\pi}\int dw' e^{iw'\eta}\, G_0^{\sigma}(\vec{r},\vec{r}';w+w')v(\vec{r},\vec{r}'), \tag{3.67}$$

for which $W(\vec{r},\vec{r}';w) = W_c(\vec{r},\vec{r}';w) + v(\vec{r},\vec{r}')$ [109,110,112].

The correlation part of the self-energy is dynamical quantity due to its frequency dependence, while the exchange part corresponds to the non-local exchange potential in the Hartree-Fock model.

As it is stated earlier, the reason for using the *GW* approximation is the fact that the DFT calculations in the ground state overestimate or underestimate the band gap values of materials. The valence and conduction bands around the Fermi level is highly critical in material classification. Consequently, if the *GW* calculations, which are computationally expensive, were not done with large number of k-points in the Brillouin zone, the band structure would not look continuous and clear. This problem is circumvented by invoking the Wannier functions, which are constructed from the Fourier transformation of Bloch functions. In contrast to Bloch functions, Wannier functions are delocalized in the reciprocal space but localized in real space [125]. This fact actually is a natural consequence of Heisenberg's uncertainty principle.

$$w_{\vec{R}j}(\vec{r}) = \frac{1}{N}\sum_{\vec{k}} e^{-i\vec{k}\cdot\vec{R}} \sum_{i} U_{\vec{k}ij}\phi_{\vec{k}i}(\vec{r}), \qquad 3.68$$

where $\phi_{\vec{k}i}(\vec{r})$ is the Bloch function, $U_{\vec{k}ij}$ is a unitary transformation matrix, and N is the number of k-vectors [125–127]. Unitary matrix is important to maintain the set of Wannier functions orthonormal, and is obtained from the projection of Bloch states onto the specified localized orbitals [125–127].

We should also note that the DFT considers, or sum over all, occupied states. On the other hand, since *GW* is for the excited states, one needs to consider also unoccupied states at higher energies. Therefore, for a specific k-point grid one needs enough number of empty bands to have reliable values for the *GW* energy band gaps. As the grid becomes denser the band gap may become smaller or larger, depending on the material.

In the one-shot *GW*, the sum in the self-energy is done only over the diagonal terms, and available KS wavefunctions are used. However, in the full-*GW* approximation, all, diagonal plus off-diagonal, elements of the self-energy matrix

are taken into account. At every k-point the wavefunctions and their corresponding eigenvalues calculated self-consistently. As expected, the full-*GW* calculations are computationally more expensive than one-shot *GW* computations.

4 RESULTS

For our calculations, we considered six quaternary Heusler (QH) alloys with XX'YZ chemical formula. We placed atoms X at 4a, X' at 4b, Y at 4c, and Z at 4d in the unit cell to have energetically most stable configuration of the QH alloys. The points we deliberate in material selection are that the compounds should have thermodynamic and mechanical stability. Furthermore, all of the materials must have been predicted to show SGS behaviour in previous studies, see Table *4.1* [36,128].

Table 4.1: The computed lattice constant, number of valence electrons N_V, total magnetic moment M_{tot}, and distance to the convex Hull of the QH materials studied.

Compound	a (Å)	N_V	M_{tot} (μ_B)	E_{con} (eV/atom)
FeVTiSi	5.91	21	3.00	0.173
FeVNbAl	6.11	21	2.99	0.1238
FeCrTiAl	5.96	21	3.00	0.0504
FeCrZrAl	6.194	21	3.00	0.0114
NiCrMnAl	5.809	26	2.00	0.1173
NiFeMnAl	5.731	28	4.00	0.0577

We start our calculations with specifying the equilibrium lattice constant, atoms and their positions in the unit cell in the input generator for FLEUR. This generator produces necessary files for the self-consistent calculation. We preferred a 20x20x20 k-point mesh and the angular momentum cutoff parameter l_{max} = 10. Then, we used relations 3.55 and 3.56 between the MT radius, and cut-off parameters for the planewave and angular momentum to determine the planewave cut-off parameters for each material. Thus, we set k_{max} = 4.00 bohr^{-1} for FeCrZrAl, but k_{max} = 4.25 bohr^{-1} for NiFeMnAl, NiCrMnAl, FeVTiSi, FeVNbAl, and FeCrTiAl. We also set G_{max}=G_{maxXC} =3k_{max} for all materials. Having finished the self-consistent calculation, we further computed the density of states (DOS) and band structure of materials. The parametrization by Perdew, Burke and Ernzerhof (PBE) under the GGA functionals was chosen to approximate the exchange-correlation potential. After the ground-state calculations, we moved forward to *GW* computations with SPEX code, and produced a new k-point set for a 12x12x12 mesh in the Brillouin zone. Then, FLEUR was run

to obtain the Kohn-Sham eigenfunctions for new the k-points. After that, SPEX was re-run and one-shot *GW* computation was performed. In this step, we set the cut-off parameter of angular momentum for products of the functions in the MT sphere L_{CUT} = 4, and reciprocal cut-off radius for mixed product basis (MPB) of the interstitial region G_{CUT} = 4 for the *GW* calculation. The last step in our calculation was to obtain full band structure of the system around the Fermi level by performing the Wannier interpolation with SPEX. The Wannier functions are localized in real space, more specifically at atomic sites [126]. We constructed an interpolated band structure by choosing certain localized orbitals as Wannier functions. The number of orbitals considered for the interpolation is determined by the position of band gap, i.e., in between which orbitals the band gap is located. Type of the orbitals of each atom to be used in the interpolation is determined by the orbitals making up the bands around the Fermi energy. For our materials, mainly the d-orbitals are responsible for the band gap. We also took into account the p-orbitals of the sp-element due to the interactions between this element and TMs. In the following sections, the DOS and the spin-polarized electronic band structures obtained by the DFT and *GW* approximation will be discussed.

4.1 Density of States (DOS) Results

We computed the DOS of the SGS candidates with FLEUR. In all calculations we considered 1000 k-points, and set the standard deviation to σ = 0.0015.

Figure 4.1 displays the spin-resolved DOS for compound FeVTiSi. We see that bottom of the CB in the spin-down channel touches top of the VB of the spin-up channel at Fermi level. According to this results FeVTiSi displays a type-II SGS behaviour. By examining the region just below E_F in the spin-up channel, one can observe the interaction between Fe-d states and V-d states. Moreover, V-d states are dominant in the VB of spin-up channel and the CB of spin-down channel.

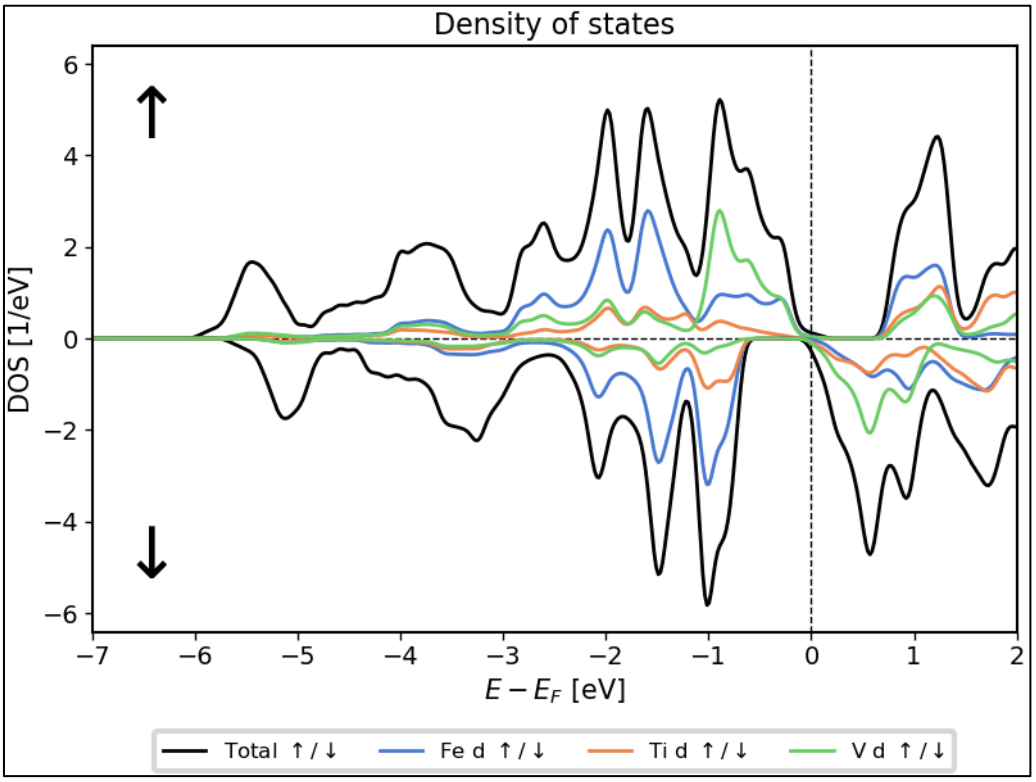

Figure 4.1 The DOS of FeVTiSi

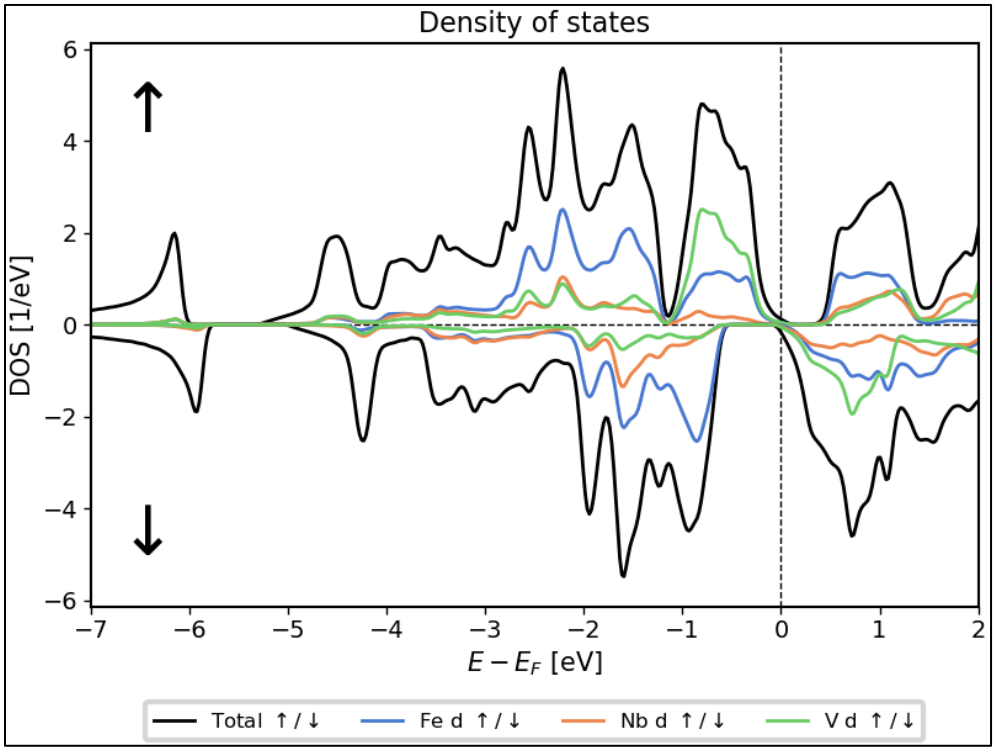

The

Figure 4.2 The DOS analysis of FeVNbAl

DOS of FeVNbAl compound is indicated in Figure 4.2. The total DOS in both spin channels displays behaviour similar to FeVTiSi in figure 4.1. The gapless structure is reached by contributions of both spin states. As the VB of the spin-up state and CB of the spin-down state touch, there are gaps around E_F. One gap is located in between the CB bottom and the Fermi level, while the other is in between the VB top and E_F in the spin-up and spin-down channels, respectively. The curves of V-d and Fe-d orbitals shows that there is a strong hybridization between these orbitals.

The DOS of FeCrTiAl is demonstrated in figure 4.3. While he CB of spin-down channel touches the Fermi level, there exists a gap between top of the VB and Fermi level. Total DOS value is almost zero the around E_F in the spin-up channel.

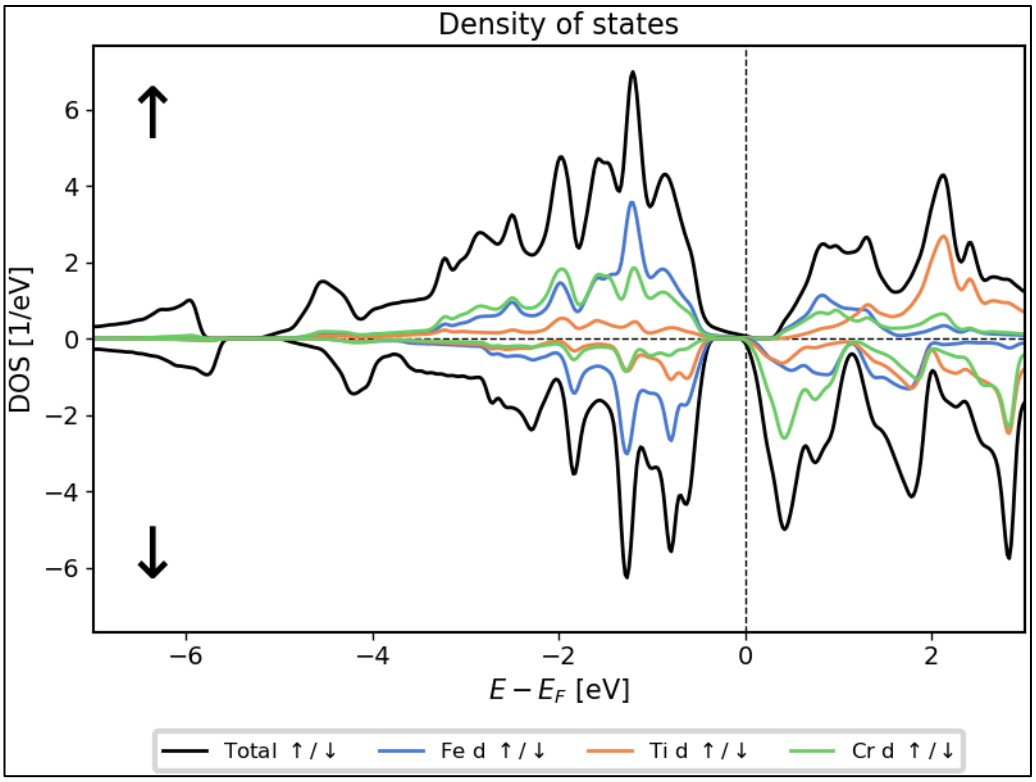

Figure 4.3The DOS analysis of FeCrTiAl

Figure 4.4 displays spin-polarized DOS FeCrZrAl. In the spin-up channel, the VB almost touches the Fermi energy, and there is a small gap between the CB and E_F. The gap in the spin-down channel is larger than in the spin-up one.

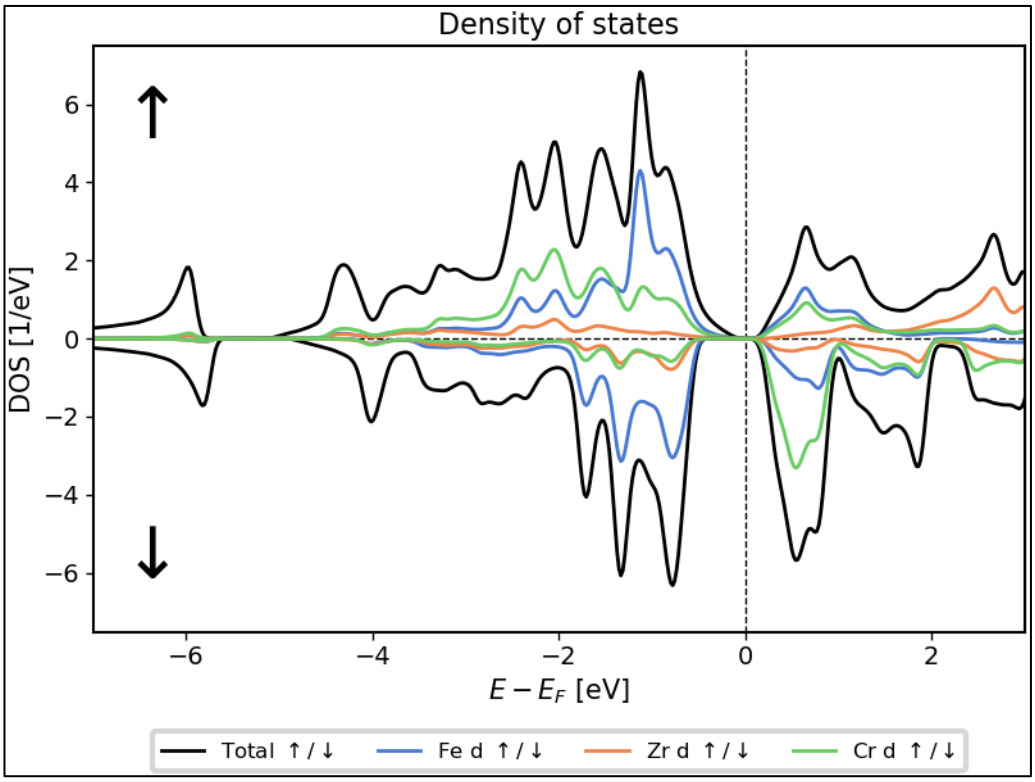

Figure 4.4The DOS plot of FeCrZrAl

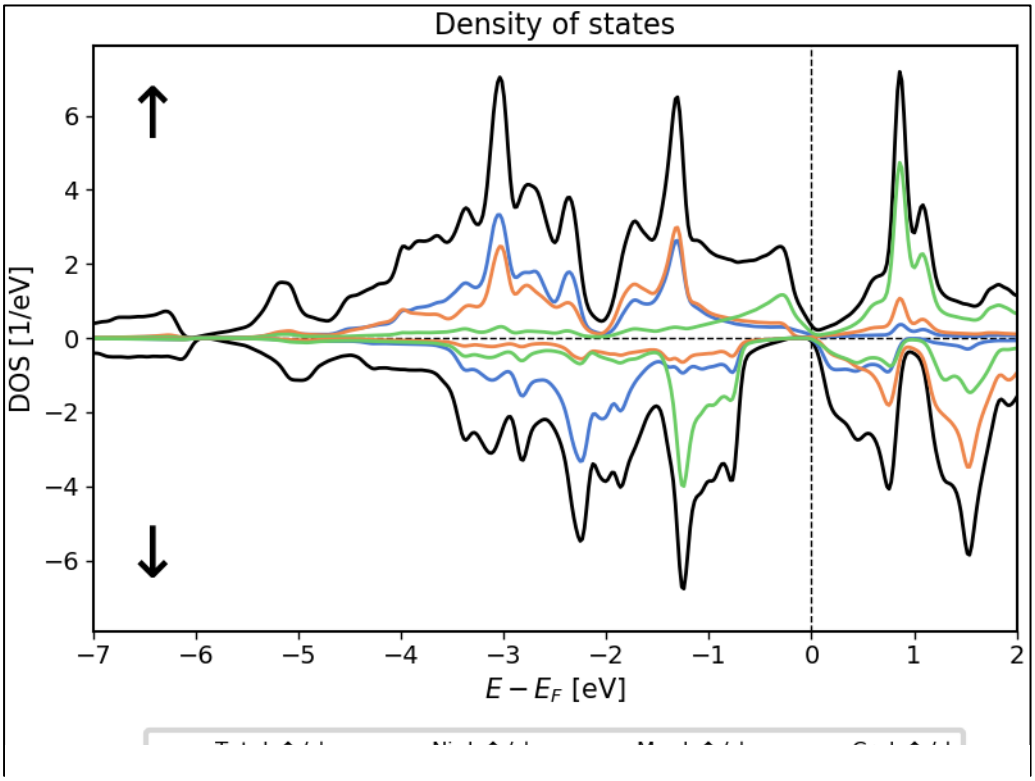

Figure 4.5 The DOS of NiCrMnAl

The DOS of NiCrMnAl is plotted in Figure 4.5. Total DOS value for spin-down channel is zero in the energy interval -0.6 - 0 eV implying that the band gap is formed here. Also, the CB bottom touches the Fermi energy in the spin-down channel. In the spin-up channel we observe the total DOS is very close to zero. In both spin-channels, there is hybridization between the d-states of TMs. By focusing on the behaviour of total DOS and Cr-d DOS around the Fermi energy in the spin-up channel, Cr-d states can be considered mainly responsible of the gapless form in this channel.

Fig. 4.6 shows the spin-polarized DOS for NiFeMnAl. As is seen, it shows semiconducting behaviour in the spin-down channel, and almost zero DOS at the Fermi energy in the spin-up channel. The Fe-d and Mn-d orbitals are mainly responsible for almost gapless nature in the spin-up channel. For both spin channels, there is a hybridization between d orbitals of the TMs. For instance, Fe-d and Mn-d states tend to show same behaviour just below E_F in the VB of spin-up channel. Similarly, d-states of Ni and Mn atoms close to E_F in the VB of spin-down channel hybridize.

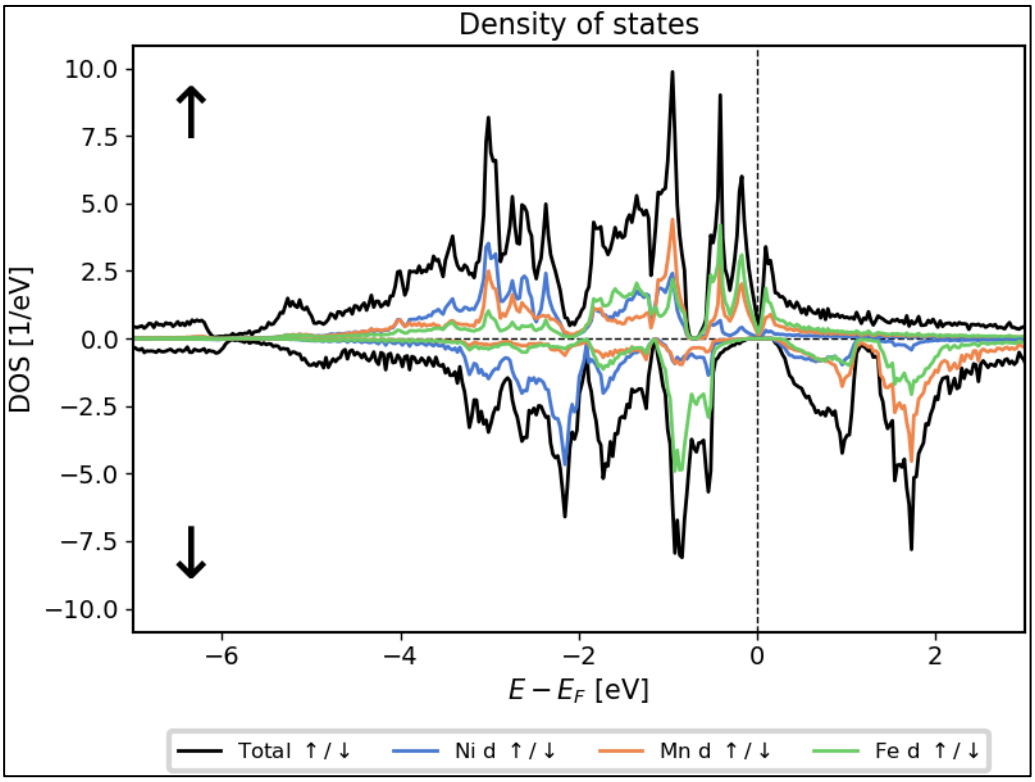

Figure 4.6 The DOS of NiFeMnAl

These DOS results confirm that all of the studied materials might be SGS as already predicted. For further analysis, in the next section we will present the band structures of the compounds computed via the PBE and *GW* methods.

4.2 Band Structures Using DFT and GW Methods

In order to make sure that our materials display SGS properties, we computed their electronic band structure first with FLEUR at the levels of KS DFT and with SPSEX at the one-shot *GW* level. Actually, SPEX gives us both Kohn-Sham and *GW* band structures after a Wannier interpolation. In the following, band structures of spin-up and spin-down channels of each material will be present separately. We set the Fermi energy at the top of the VB of the spin-up channel. The band structures computed with FLEUR code are presented in the Appendices.

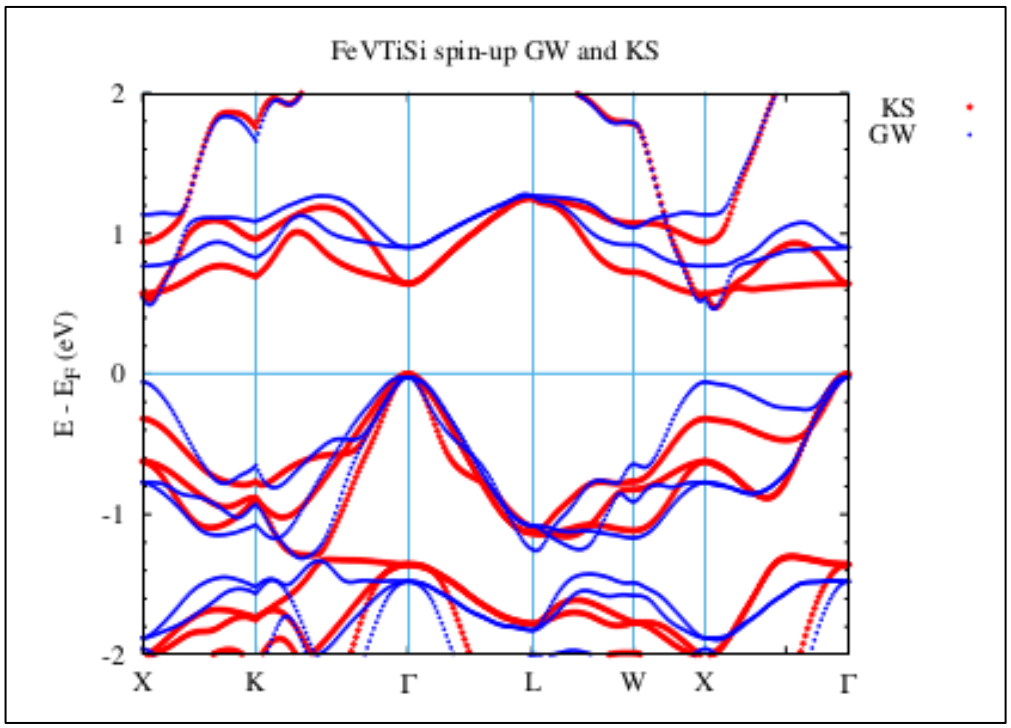

Figure 4.7Electronic band structure of FeVTiSi in the spin-up channel.

Figure 4.7 displays the band-structure of spin-up electrons in FeVTiSi. We observe that the maximum of the VB is around the midpoint between the Γ and L points. Both *GW* and KS predict an indirect band gap for this channel of about 0.42 eV. As usual, *GW* energies in the CB are shifted up.

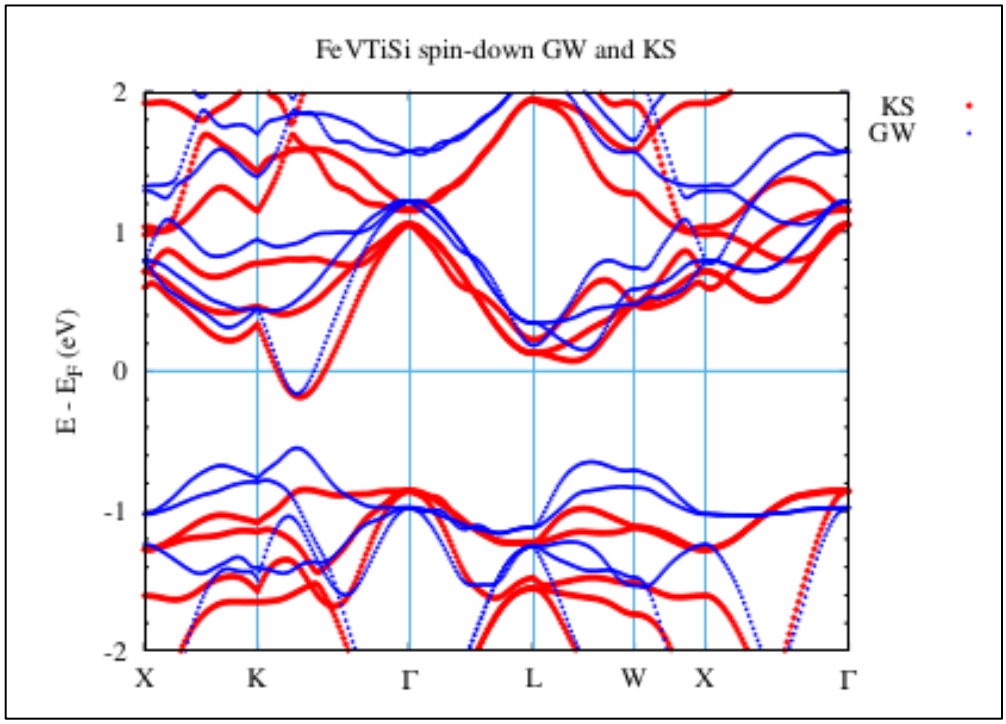

Figure 4.8 Spin-down band structure of FeVTiSi

In Figure 4.8, we observe that the CB crosses the Fermi level up to 0.2 eV in the spin-down channel. The band gap in the *GW* is direct and around 0.4 eV. One can thus conclude that FeVTiSi is a narrow band gap SGS.

Band structures of FeVNbAl spin-up states are shown in Fig. 4.9. It is noticed that there is a small overlap between the conduction and valence bands of *GW* approximation between points X and Γ. For the spin-down channel, band structure obtained via *GW* method has a very small band gap between K and Γ points around E_F (see Fig. 4.10). Below the Fermi level, the *GW* bands are shifted upwards with respect to the KS bands. These observations tell us that the *GW* predicts FeVNbAl as a SGS unlike PBE, which predicts it as a semiconductor.

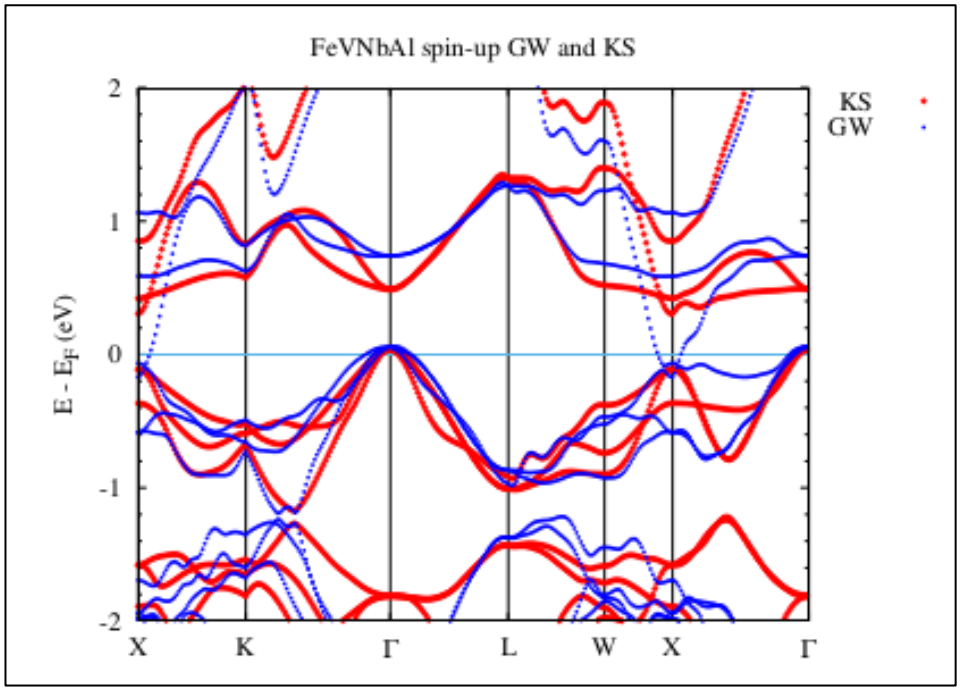

Figure 4.9spin-up band-structure of FeVNbAl

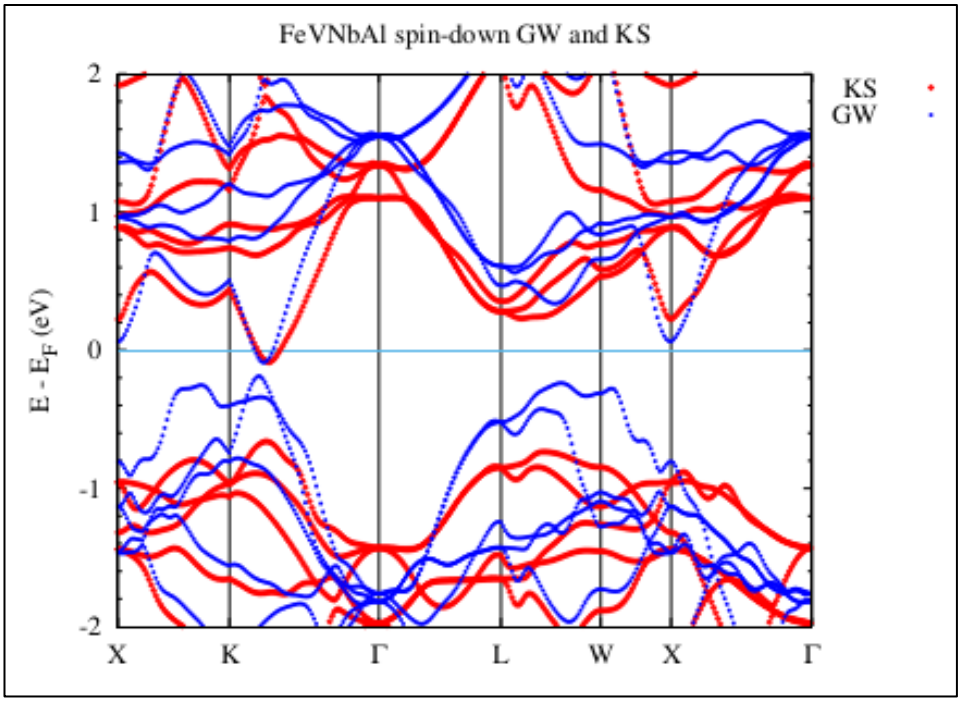

Figure 4.10 Spin-down band-structure of FeVNbAl

We plotted the band diagram for spin-up channel of FeCrTiAl in Fig. 4.11. Starting with the CB there is an upward shift in the blue curves with respect to the red curves, a typical result of *GW* approximation, meaning a larger band gap energy in the *GW*. Corresponding Wannier interpolation for FeCrTiAl spin-down channel is demonstrated in Fig. 4.12. The bands close to the Fermi energy have similar behaviour with the associated spin channel of FeVTiSi. If one takes a closer look around the Fermi level, the minimum of CB has quite small lower energies than E_F. Besides the band gap is decreases in the *GW*. Based on these results, we theoretically verify that FeCrTiAl is a narrow band gap SGS.

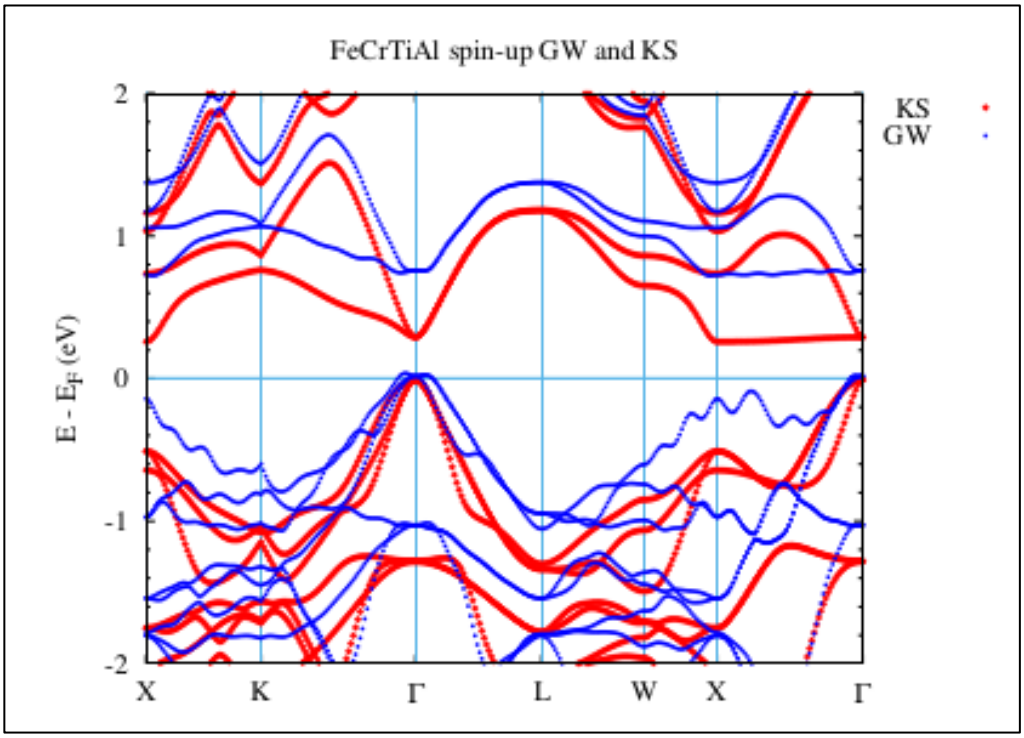

Figure 4.11 Spin-up band-structure of FeCrTiAl

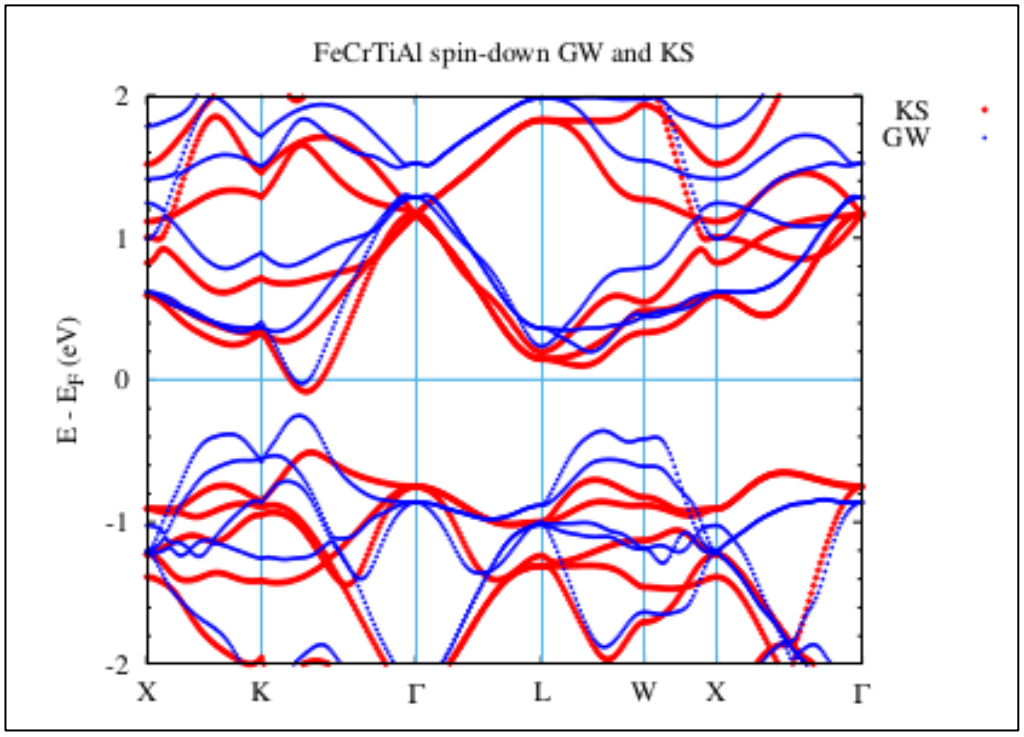

Figure 4.12 FeCrTiAl spin-down channel

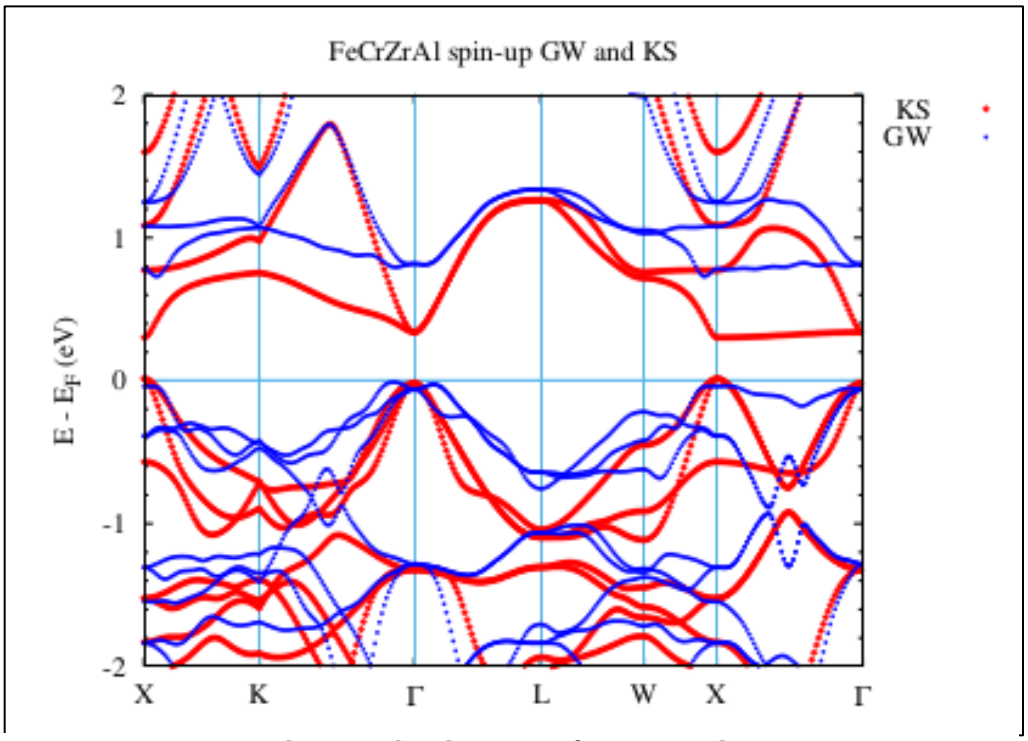

Figure 4.13 Electronic band structure for FeCrZrAl spin-up states

Figs. 4.13 and 4.14 display the spin-polarized band diagrams of FeCrZrAl. Starting with spin-up states, we see that the *GW* bands are pushed to upper energies above the Fermi level. The KS has a direct band gap of almost 0.2 eV in the X - Γ direction. On the other hand, *GW* has a direct band gap of about 0.8 eV around

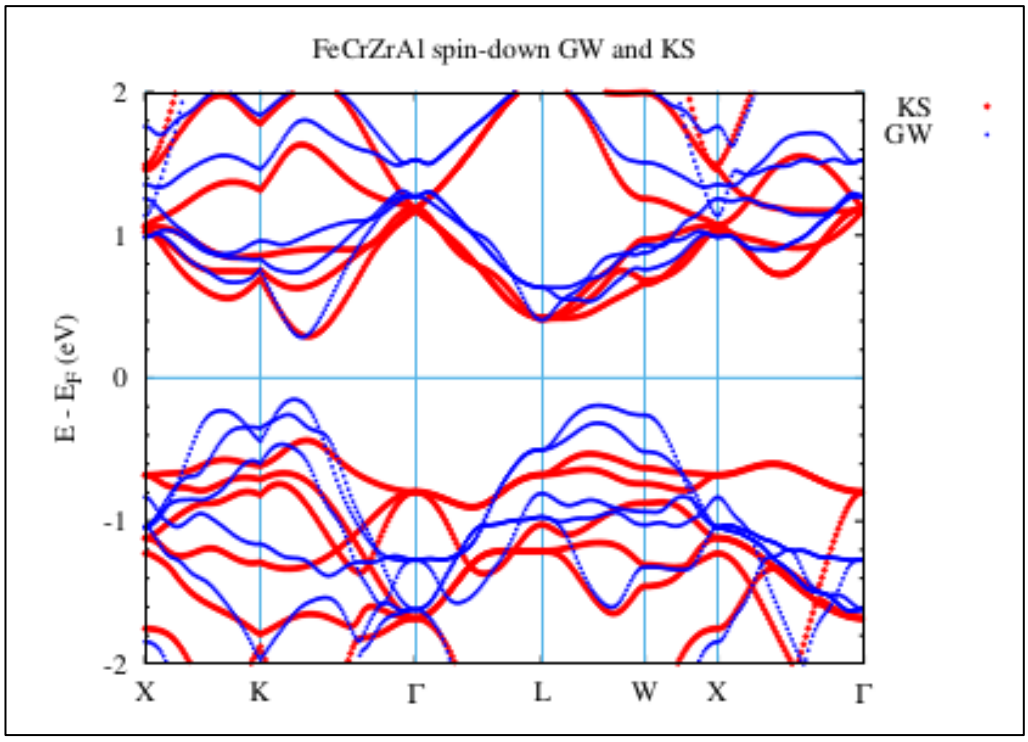

Figure 4.14 FeCrZrAl spin-down states electronic band diagram

middle of the Γ and L points. As is seen in Fig. 4.14, for the spin-down channel the *GW* valence bands are closer to the Fermi level than the KS bands for the spin-down channel. Bottom of the CB in both methods coincides between the points K and Γ. Taking into account behaviour of the bands in both spin-channels, we can deduce that FeCrZrAl is a narrow band gap semiconductor of SGS.

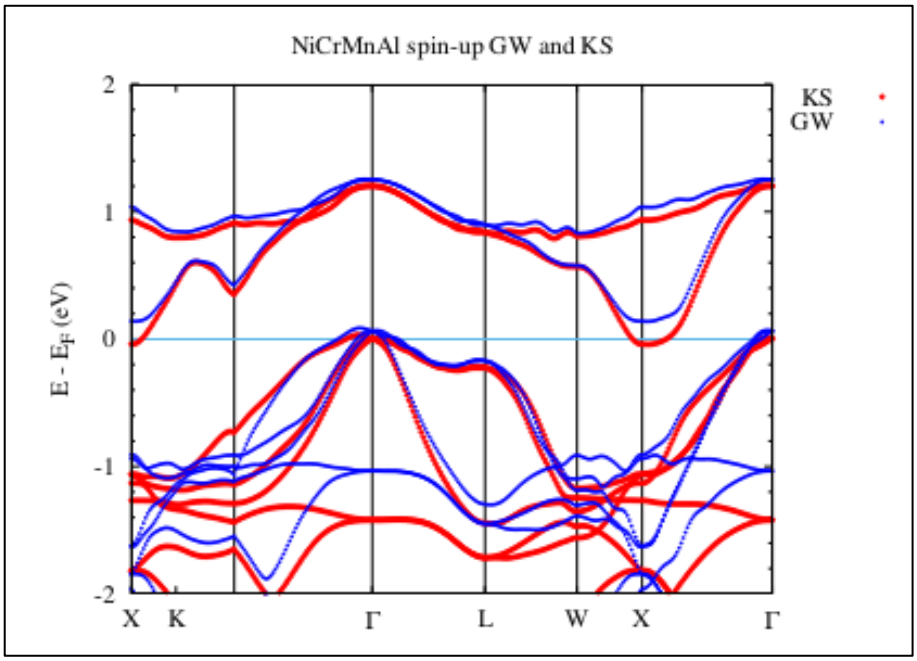

Figure 4.15 NiCrMnAl spin-up states

The CB top is in between the Γ and L points in the spin-up channel of NiCrMnAl as observed in Fig. 4.15. The eigenvalues in the CB of *GW* are shifted very slightly to higher energies and thus a slight bandgap energy of about 0.2 eV opens in the *GW*. We notice that the KS band structure is gapless.

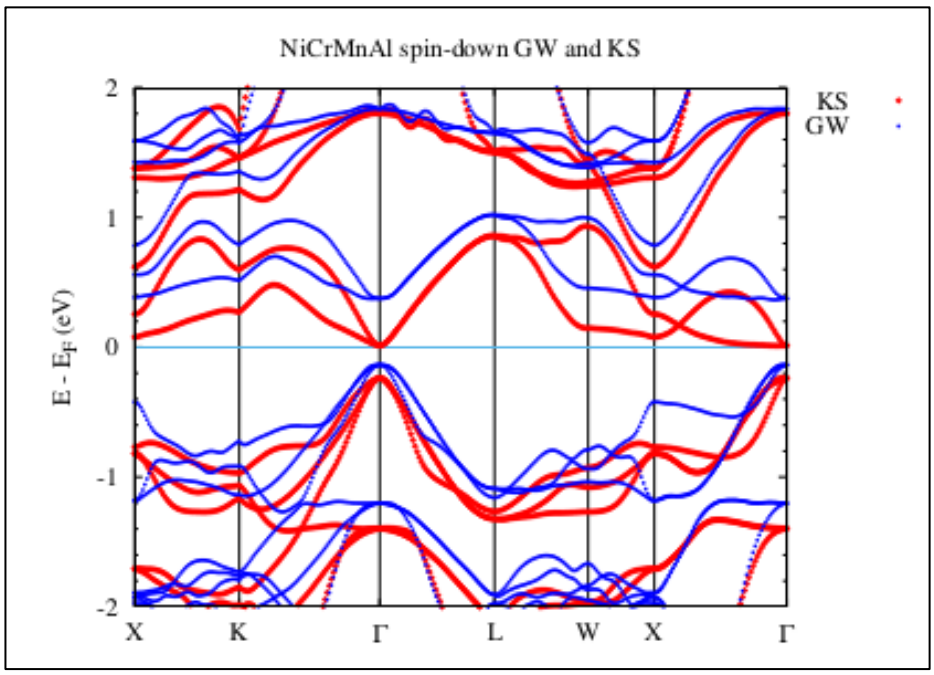

Figure 4.16 NiCrMnAl spin-down states

In Fig. 4.16 we observe that the spin-down channel has a direct band gap of 0.2 eV in the middle of Γ to L points. Overall, the *GW* eigenvalues shift to lower energies compared to KS results. We may conclude that NiCrMnAl is a SGS in the PBE, and a narrow bandgap SGS in the *GW* theory.

The band structure for spin-up electrons of NiFeMnAl in Fig. 4.17. The Wannier-interpolated band structure provides a good understanding of the bands centring E_F. The VB touches the Fermi level at the middle of the high symmetry points K and Γ. Also, the CB touches the Fermi level at a point close to X point. We observe that the Kohn-Sham and *GW* energies are almost the same around Fermi energy.

In the spin-down channel, Fig. 4.16, the VB top is around the middle of the path from Γ to L point, and the *GW* energy is lower than of KS approximately 0.2 eV. There is an indirect bandgap of almost 0.3 eV in this channel. Combining the observations for both spin channels we conclude that NiFeMnAl is a SGS material.

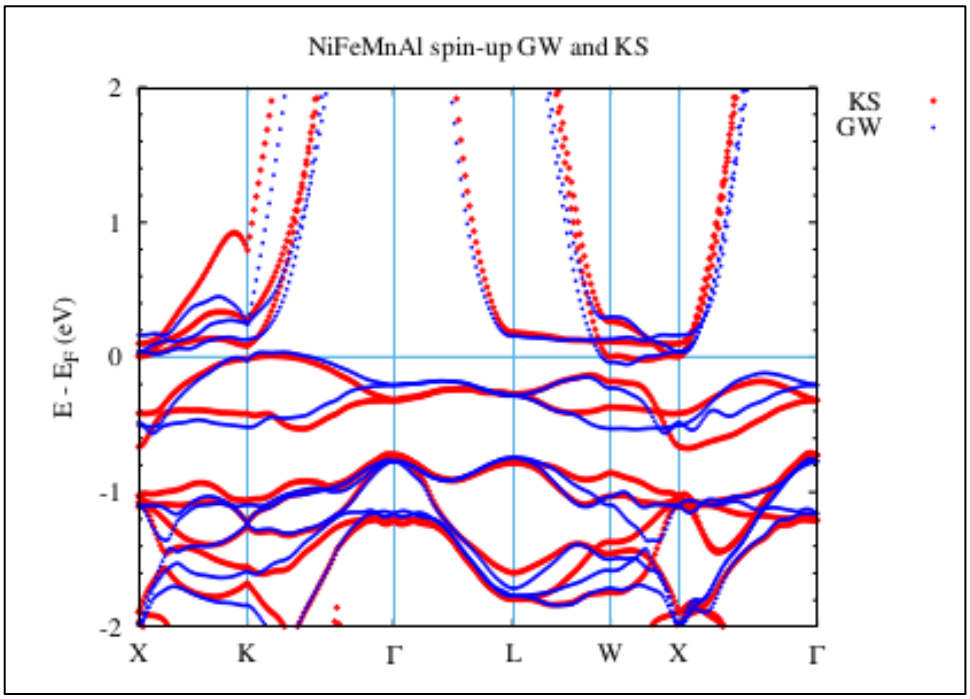

Figure 4.17 NiFeMnAl spin-up states

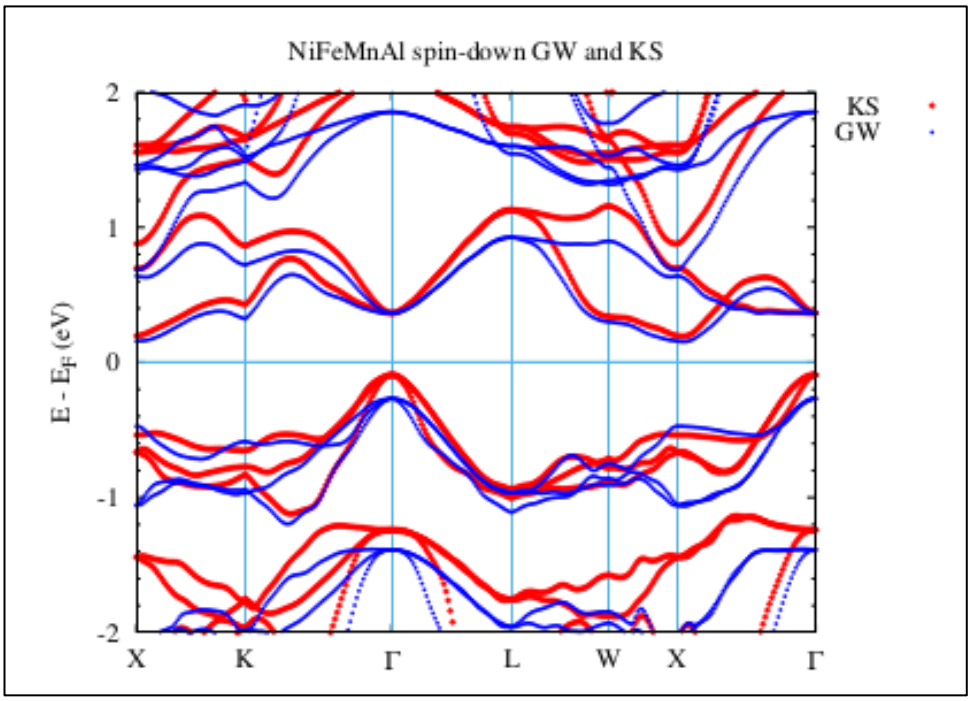

Figure 4.18 NiFeMnAl spin-down states

5 CONCLUSION

In this thesis we searched for new spin-gapless semiconductor (SGS) quaternary Heusler materials within the DFT and GW methods. We conclude that FeVTiSi, FeVNbAl, FeCrTiAl, FeCrZrAl, NiCrMnAl and NiFeMnAl can be classified as SGS. In these materials the difference of the KS DFT and one-shot *GW* are, in general, close to each other. This fact implies that in these systems the many-body correlations have a minimal effect on the electronic band structure.

REFERENCES

[1] Neamen D. A., (2012), “Semiconductor physics and devices: basic principles”, McGraw-Hill.

[2] Grundmann M., (2016), “The Physics of Semiconductors: An Introduction Including Nanophysics and Applications”, Springer.

[3] Kilby J., (1964), “Miniaturized Electronic Circuits”, US3138743A.

[4] Moore G. E., (1995), “Lithography and the Future of Moore’s Law”, SPIE Vol. 2437.

[5] Moore G. E., (1965), “Cramming More Components onto Integrated Circuits”, Electronics, 38(8), 1–14.

[6] Moore G. E., (1975), “Progress in Digital Integrated Electronics”, Technical Digest Int’l Electron Devices Meeting, 21, 11–3.

[7] Intel Processors Over The Years, (2023), https://www.businessnewsdaily.com/10817-slideshow-intel-processors-over-the-years.html , (Accessed: 03/02/2023).

[8] Apple unveils M2 Pro and M2 Max: next-generation chips for next-level workflows, (2023), https://www.apple.com/newsroom/2023/01/apple-unveils-m2-pro-and-m2-max-next-generation-chips-for-next-level-workflows/#:~:text=M2%20Pro%20scales%20up%20the,to%2096GB%20of%20unified%20memory. , (Accessed: 03/02/2023).

[9] Theis T. N. and Solomon P. M., (2010), “In quest of the next switch: Prospects for greatly reduced power dissipation in a successor to the silicon field-effect transistor”, Proceedings of the IEEE vol 98 (Institute of Electrical and Electronics Engineers Inc.), 2005–14.

[10] Sze S. M. and Lee M. K., (2012), “Semiconductor Devices Physics and Technology”, Wiley.

[11] The Tunneling Transistor, (2013), https://spectrum.ieee.org/the-tunneling-transistor , (Accessed: 03/02/2023).

[12] Theis T. N. and Philip Wong H. S., (2017), “The End of Moore’s Law: A New Beginning for Information Technology”, Comput Sci Eng, 19, 41–50.

[13] Grundmann M., (2016), The Physics of Semiconductors, Springer International Publishing.

[14] Landauer R., (1961), ‘Irreversibility and Heat Generation in the Computing Process”, IBM Journal, 183–91.

[15] Ionescu A. M. and Riel H., (2011), “Tunnel field-effect transistors as energy-efficient electronic switches”, Nature, 479, 329–37.

[16] Landau L. D. and Lifshitz E. M., (1965), Quantum Mechanics: Non-relativistic Theory vol 3, Pergamon Press.

[17] Schiff L. I., (1968), Quantum Mechanics, McGraw-Hill Book Company.

[18] 1953: Whirlwind computer debuts core memory, (2015), https://www.computerhistory.org/storageengine/whirlwind-computer-debuts-core-memory/ , (Accessed: 03/08/2023).

[19] Magnetic Core Memory, https://www.computerhistory.org/revolution/memory-storage/8/253 , (Accessed: 03/08/2023).

[20] Advanced Information, (2007), https://www.nobelprize.org/prizes/physics/2007/advanced-information/ , (Accessed: 03/19/2023).

[21] The Nobel Prize in Physics, (2007), https://www.nobelprize.org/prizes/physics/2007/summary/ , (Accessed: 03/19/2023).

[22] Chang L., Wang M., Liu L., Luo S., & Xiao P., (2014), "A brief introduction to giant magnetoresistance", arXiv:1412.7691.

[23] Zayets V., (2018), "Spin transport of electrons and holes in a metal and in a semiconductor", Journal of Magnetism and Magnetic Materials, 445, 53-65.

[24] Zuti I., Fabian J., & Das Sarma S., (2004), "Spintronics: Fundamentals and applications", Rev. Mod. Phys., 76(2), 323-410.

[25] Wolf S. A., Awschalom D. D., Buhrman R. A., Daughton J. M., Von Molnár S., Roukes M. L., Chtchelkanova A. Y., & Treger D. M., (2001), "Spintronics: A Spin-Based Electronics Vision for the Future", Science, 294, 1488–95.

[26] Davidson A., Amin V. P., Aljuaid W. S., Haney P. M., & Fan X., (2020), "Perspectives of Electrically generated spin currents in ferromagnetic materials", Physics Letters A, 384(11), 126228.

[27] Li X., & Yang J., (2016), "First-principles design of spintronics materials", Natl Sci Rev, 3, 365–81.

[28] Dilute Magnetic Semiconductors, (2009), https://warwick.ac.uk/fac/sci/physics/current/postgraduate/regs/mpagswarwick/ex5/intro/iii-v-compoundsemiconductors/dms/ , (Accessed: 03/25/2023).

[29] de Groot R. A., Mueller F. M., Van Engen P. G., & Buschow K. H. J., (1983), "New Class of Materials: Half-Metallic Ferromagnets", Phys. Rev. Lett., 50, 2024–7.

[30] Galanakis I., Dederichs P. H., & Papanikolaou N., (2002), "Slater-Pauling behavior and origin of the half-metallicity of the full-Heusler alloys", Phys. Rev. B, 66, 1–9.

[31] Wang X. L., (2008), “Proposal for a new class of materials: Spin gapless semiconductors”, Phys. Rev. Lett., 100.

[32] Ouardi S., Fecher G. H., Felser C., & Kübler J., (2013), “Realization of spin gapless semiconductors: The Heusler compound Mn2CoAl”, Phys. Rev. Lett., 110.

[33] Rani D., Bainsla L., Alam A., & Suresh K. G., (2020), “Spin-gapless semiconductors: Fundamental and applied aspects”, J. Appl. Phys., 128.

[34] Wang X. L., Dou S. X., & Zhang C., (2010), “Zero-gap materials for future spintronics, electronics and optics”, NPG Asia Mater., 2, 31–8.

[35] Yue Z., Li Z., Sang L., & Wang X., (2020), “Spin-Gapless Semiconductors”, Small, 16.

[36] Gao Q., Opahle I., & Zhang H., (2019), “High-throughput screening for spin-gapless semiconductors in quaternary Heusler compounds”, Phys. Rev. Mater., 3.

[37] Bainsla L., Mallick A. I., Raja M. M., Nigam A. K., Varaprasad B. S. D. Ch. S., Takahashi Y. K., Alam A., Suresh K. G., & Hono K., (2015), “Spin gapless semiconducting behavior in equiatomic quaternary CoFeMnSi Heusler alloy”, Phys. Rev. B, 91.

[38] Tsidilkovski I. M., (2011), “Electron Spectrum of Gapless Semiconductors”, Springer Berlin, Heildelberg.

[39] Wang X., Peleckis G., Zhang C., Kimura H., & Dou S., (2009), “Colossal electroresistance and giant magnetoresistance in doped PbPdO 2 thin films”, Advanced Materials, 21, 2196–9.

[40] Han Y., Khenata R., Li T., Wang L., & Wang X., (2018), “Search for a new member of parabolic-like spin-gapless semiconductors: The case of diamond-like quaternary compound CuMn2InSe4”, Results Phys, 10, 301–3.

[41] Lei J., Xu M. C., & Hu S. J., (2017), “Anchoring transition metal elements on graphene-like ZnO monolayer by CO molecule to obtain spin gapless semiconductor”, Appl. Surf. Sci., 416, 681–5.

[42] Felser C., Wollmann L., Chadov S., Fecher G. H., & Parkin S. S. P., (2015), “Basics and prospective of magnetic Heusler compounds”, APL Mater, 3.

[43] Graf T., Felser C., & Parkin S. S. P., (2011), “Simple rules for the understanding of Heusler compounds”, Progress in Solid State Chemistry, 39, 1–50.

[44] Felser C., & Hirohata A., “Heusler Alloys Properties, Growth, Applications”, Springer Series in Materials Science, 222.

[45] Bradley A. J., & Rodgers J. W., (1934), “The Crystal Structure of the Heusler Alloys”, Royal Society, 144(852), 340-359.

[46] Wang X., Cheng Z., Wang J., Wang X. L., & Liu G., (2016), "Recent advances in the Heusler based spin-gapless semiconductors", J. Mater. Chem. C, 4, 7176–92.

[47] Fan X., Li J., & Jin Y., (2018), "Effects of strain on the half-metallicity and spin gapless feature of Ti2 y Si (Y = Fe, Co) alloys", Modern Physics Letters B, 32.

[48] Mehl M. J., Hicks D., Toher C., Levy O., Hanson R. M., Hart G., & Curtarolo S., (2017), "The AFLOW Library of Crystallographic Prototypes: Part 1", Comput. Mater. Sci., 136, S1–828.

[49] Hicks D., Mehl M. J., Gossett E., Toher C., Levy O., Hanson R. M., Hart G., & Curtarolo S., (2019), "The AFLOW Library of Crystallographic Prototypes: Part 2", Comput. Mater. Sci., 161, S1–1011.

[50] Hicks D., Mehl M. J., Esters M., Oses C., Levy O., Hart G. L. W., Toher C., & Curtarolo S., (2021), "The AFLOW Library of Crystallographic Prototypes: Part 3", Comput. Mater. Sci., 199, 110450.

[51] Williams A. R., Moruzzi V. L., Malozemoff A. P., & Terakura K., (1983), "Generalized Slater-Pauling Curve for Transition Metal Magnets", IEEE Transactions on Magnetics, 19(5).

[52] Kübler J., (1984), "First principle theory of metallic magnetism", Physica B+C ,127, 257–63.

[53] Dresselhaus M. S., Dresselhaus G., & Jorio A., (2008), "Group Theory Application to the Physics of Condensed Matter", Springer.

[54] Galanakis I., Mavropoulos P., & Dederichs P. H., (2006), "Electronic structure and Slater-Pauling behaviour in half-metallic Heusler alloys calculated from first principles" J. Phys. D. Appl. Phys., 39, 765–75.

[55] Blundell S., (2001), "Magnetism in Condensed Matter", Oxford University Press.

[56] Rai D. P., & Thapa R. K., (2012), "A First Principle Calculation of Full-Heusler Alloy Co 2 TiAl: LSDA+ U Method", ISRN Condensed Matter Physics, 2012, 1–5.

[57] Xu G. Z., Liu E. K., Du Y., Li G. J., Liu G. D., Wang W. H., & Wu G. H. A., (2013), "A New Spin Gapless Semiconductors Family: Quaternary Heusler Compounds", Europhysics Letters, 102(1).

[58] Skaftouros S., Özdoğan K., Şaşioğlu E., & Galanakis I., (2013), "Generalized Slater-Pauling rule for the inverse Heusler compounds", Phys. Rev. B, 87.

[59] Zhang Y. J., Liu Z. H., Liu E. K., Liu G. D., Ma X. Q., & Wu G. H., (2015), "Towards fully compensated ferrimagnetic spin gapless semiconductors for spintronic applications", EPL, 111.

[60] Wang X., Cheng Z., Zhang G., Yuan H., Chen H., & Wang X. L., (2020), "Spin-gapless semiconductors for future spintronics and electronics", Phys Rep, 888, 1–57.

[61] Luo H., Xin Y., Liu B., Meng F., Liu H., Liu E., & Wu G., (2016), "Competition of L21 and XA structural ordering in Heusler alloys X2CuAl (X = Sc, Ti, V, Cr, Mn, Fe, Co, Ni)", J Alloys Compd, 665, 180–5.

[62] Taş M., Şaşıoğlu E., Friedrich C., & Galanakis I., (2017), "A first-principles DFT+GW study of spin-filter and spin-gapless semiconducting Heusler compounds", Journal of Magnetism and Magnetic Materials, 441, 333-8.

[63] Jia H. Y., Dai X. F., Wang L. Y., Liu R., Wang X. T., Li P. P., Cui Y. T., & Liu G. D., (2014), "Ti2Mn Z (Z =Al, Ga, In) compounds: Nearly spin gapless semiconductors", AIP Adv, 4(4).

[64] Klaer P., Balke B., Alijani V., Winterlik J., Fecher G. H., Felser C., & Elmers H. J., (2011), "Element-specific magnetic moments and spin-resolved density of states in CoFeMnZ (Z=Al, Ga; Si, Ge)", Phys. Rev. B., 84.

[65] Alijani V., Ouardi S., Fecher G. H., Winterlik J., Naghavi S. S., Kozina X., Stryganyuk G., Felser C., Ikenaga E., Yamashita Y., Ueda S., & Kobayashi K., (2011), "Electronic, structural, and magnetic properties of the half-metallic ferromagnetic quaternary Heusler compounds CoFeMnZ (Z=Al, Ga, Si, Ge)", Phys. Rev. B., 84.

[66] Özdoğan K., Şaşıoğlu E., & Galanakis I., (2013), "Slater-Pauling behavior in LiMgPdSn-type multifunctional quaternary Heusler materials: Half-metallicity, spin-gapless and magnetic semiconductors", J. Appl. Phys., 113.

[67] Alijani V., Winterlik J., Fecher G. H., Naghavi S. S., & Felser C., (2011), "Quaternary half-metallic Heusler ferromagnets for spintronics applications", Phys. Rev. B., 83.

[68] Taş M., Şaşıoğlu E., Galanakis I., Friedrich C., & Blugel S., (2016), "Quasiparticle Band Structure Of The Almost-Gapless Transition-Metal-Based Heusler Semiconductors", Phys. Rev. B.

[69] Zhang Y. J., Liu Z. H., Wu Z. G., & Ma X. Q., (2019), "Prediction of fully compensated ferrimagnetic spin-gapless semiconducting FeMnGa/Al/In half Heusler alloys", IUCrJ, 6, 610–8.

[70] Jiao Y., (2018), "Computational Discovery and Electronic Engineering in Nanomaterials for Photovoltaic and Electronic Applications", PhD Thesis, Queensland University Of Technology.

[71] Wang X. L., (2017), "Dirac Spin Gapless Semiconductors: Ideal Platforms For Massless And Dissipationless spintronics And New (Quantum) Anomalous Spin Hall Effects", Natl. Sci. Rev., 4, 252–7.

[72] Wang X., Li T., Cheng Z., Wang X. L., & Chen H., (2018), "Recent Advances In Dirac Spin-Gapless Semiconductors", Appl. Phys. Rev., 5.

[73] Davatolhagh S., & Dehghan A., (2018), “Dirac-Like Half-Metallicity Of d0−d Half-Heusler Alloys”, Physica C: Superconductivity and its Applications, 552, 53–6.

[74] Davatolhagh S., & Dehghan A., (2017), “d0-d Half-Heusler Alloys: A Class Of Future Spintronic Materials”, arXiv:1701.08397.

[75] Dehghan A., & Davatolhagh S., (2019), “d0-d Half-Heusler Alloys: A Potential Class Of Advanced Spintronic Materials”, J. Alloys Compd., 772, 132–9.

[76] Tomar S., Ghosh B., Mardanya S., Rastogi P., Bhadoria B., Chauhan Y. S., Agarwal A., & Bhowmick S., (2019), “Intrinsic Magnetism In Monolayer Transition Metal Trihalides: A Comparative Study”, Journal of Magnetism and Magnetic Materials, 489.

[77] McGuire M. A., (2017), “Crystal and Magnetic Structures in Layered, Transition Metal Dihalides and Trihalides”, Crystals, 7(5), 121.

[78] He J., Ma S., Lyu P., & Nachtigall P., (2016), “Unusual Dirac Half-Metallicity With Intrinsic Ferromagnetism In Vanadium Trihalide Monolayers”, J. Mater. Chem. C., 4, 2518–26.

[79] Kaxiras E., & Joannopoulos J. D., (2019), “Quantum Theory Of Materials”, Cambridge University Press.

[80] Schindlmayr A., Friedrich C., Şaşıoğlu E., & Blügel S., (2011), “First-Principles Calculation of Electronic Excitations in Solids With SPEX”

[81] ab-initio calculation, Oxford Reference, https://www.oxfordreference.com/display/10.1093/oi/authority.20110803095344143 , (Accessed: 04/04/2023).

[82] Wortmann D., Helbig N., & Blügel S., (2014), “Describing Many-Electron Systems Computing Solids Models”, ab-initio methods and supercomputing, 74, 12–40.

[83] Toulouse J., (2022), “Introduction to Density-Functional Theory”, 3rd edition of the International summer School in electronic structure Theory: electron correlation in Physics and Chemistry (ISTPC), Aussois, France, 19 June - 2 July.

[84] Hartree D. R., (1928), “The Wave Mechanics of an Atom with a Non-Coulomb Central Field. Part II. Some Results and Discussion”, Mathematical Proceedings of the Cambridge Philosophical Society, 24(1), 111–32.

[85] Fock V., (1930), “Näherungsmethode zur Lösung des quantenmechanischen Mehrkörperproblems”, ZPhy., 61, 126–48.

[86] Betzinger M., (2014), “Hartree-Fock And Quantum Chemical Correlation Methods Computing Solids Models”, ab-initio methods and supercomputing, 76, 62–86.

[87] Slater J. C., (1951), “A Simplification Of The Hartree-Fock Method”, Physical Review, 81, 385–90.

[88] Harrison N. M., (2001), “An Introduction to Density Functional Theory”, Lecture Notes, Department of Chemistry, Imperial College of Science Technology and Medicine, London, the UK.

[89] Ležaić M., & Mokrousov Y., (2014), “Introduction to Density Functional Theory Computing Solids Models”, ab-initio methods and supercomputing vol 74, 41–61.

[90] Lieb E. H., (2000), “A Brief Review of Thomas-Fermi Theory”, Departments of Physics and Mathematics, Jadwin Hall, Princeton University, New Jersey, The USA.

[91] Sholl D. S., & Steckel J. A., (2009), “Density Functional Theory A Practical Introduction, John Wiley & Sons, Inc.

[92] Hohenberg P., & Kohn W., (1964), “Inhomogenous Electron Gas”, Physical Review, 136, 864–71.

[93] Levy M., (1979), “Universal Variational Functionals Of Electron Densities, First-Order Density Matrices, And Natural Spin-Orbitals And Solution Of The v-Representability Problem”, National Academy of Sciences, 76(12), 6062–5.

[94] Lieb E. H., (1983), “Density Functionals for Coulomb Systems”, Int. J. Quantum Chem., 24, 243–77.

[95] Betzinger M., (2011), “Orbital-Dependent Exchange-Correlation functionals In Density-Functional Theory Realized By The FLAPW Method”, Doctoral Dissertation, Fröndenberg: RWTH Aachen University.

[96] Kohn W., & Sham L. J., (1965), “Self-Consistent Equations Including Exchange and Correlation Effects”, Physical Review, 140, 1133–8.

[97] Blügel S., (2021), “Density Functional Theory”, FLEUR hands-on, 12-16 April.

[98] Singh D. J., & Nordström L., (2006), “Planewaves, Pseudopotentials And The LAPW Method”, Springer Science Business Media, Inc.

[99] Rappoport D., Crawford N. R. M., Furche F., & Burke K., (2008), “Which functional should I choose?”, Computational Inorganic and Bioinorganic Chemistry, Wiley.

[100] Hedin L., (1965), “New Method For Calculating The One-Particle Green’s Function With Application To The Electron-Gas Problem”, Physical Review, 139, 796–823.

[101] Schiff L. I., (1968), “Quantum Mechanics”, 3rd Edition, McGraw-Hill Inc.

[102] Golze D., Dvorak M., & Rinke P., (2019), “The GW Compendium: A Practical Guide To Theoretical Photoemission Spectroscopy”, Front. Chem., 7, 1–66.

[103] Friedrich C., & Schindlmayr A., (2014), “Many-Body Perturbation Theory: The GW Approximation Computing Solids Models”, ab-initio methods and supercomputing, 74, 87–107.

[104] Stan A., Dahlen N. E., & Van Leeuwen R., (2009), “Levels Of Self-Consistency In The GW Approximation”, Journal of Chemical Physics, 130.

[105] Aryasetiawan F., & Gunnarsson O., (1997), “The GW method”, Reports on Progress in Physics, 61(3), 237.

[106] Gatti M., (2007), “Ab-Initio Calculations Of Many body Effects In Electronic Spectre”, Ecole Polytechnique X.

[107] Toulouse J., (2019), “Introduction To Many-Body Green-Function Theory”, Lecture Notes, Laboratoire de Chimie Theorique Sorbonne Universite et CNRS, Paris, France.

[108] Tarantino W., Romaniello P., Berger J. A., & Reining L., (2017), “The Self-Consistent Dyson Equation And Self-energy Functionals: Failure Or New Opportunities?”, Phys. Rev. B, 96(4), 045124.

[109] Friedrich C., (2019), “Many-Body Perturbation Theory The GW approximation”, Picking Flowers Workshop, Jülich, Germany.

[110] Friedrich C., Blügel S., & Schindlmayr A., (2010), “Efficient Implementation Of The GW Approximation Within The All-Electron FLAPW Method”, Phys. Rev. B, 81.

[111] Bohm D., & Pines D., (1953), “A Collective Description Of Electron Interactions: III. Coulomb Interactions In A Degenerate Electron Gas”, Physical Review, 92, 609–25.

[112] Christiansson V., (2019), “The Self-Screening Correction To RPA And GW - A Model And ab initio Study”, Master’s Thesis, Lund University.

[113] The FLEUR project: www.flapw.de

[114] Weinert M., Wimmer E., & Freeman A. J., (1982), “Total-energy all-electron density functional method for bulk solids and surfaces”, Phys. Rev. B, 26, 4571–8.

[115] Blügel S., & Bihlmayer G., (2006), “Full-Potential Linearized Augmented Plane wave Method”, NIC Series, 31, 85–129.

[116] Michalicek G., (2015), “Extending The Precision And Efficiency Of The All-electron Full-potential Linearized Augmented Plane-wave Density Functional Theory Method”, Forschungszentrum Jülich GmbH, 102, 41–74.

[117] Slater J. C., (1957), “Wave Functions In A Periodic Potential”, Physical Review, 51, 846–51.

[118] Andersen K. O., (1975), “Linear Methods In Band Theory”, Phys. Rev. B, 12, 3060–83.

[119] Marcus P. M., (1967), “Variational Methods In The Computation Of Energy Bands”, Int. J. Quantum Chem., 1, 567–88.

[120] Betzinger M., Friedrich C., Blügel S., & Görling A., (2011), “Local exact exchange potentials within the all-electron FLAPW method and a comparison with pseudopotential results”, Phys. Rev. B, 83(4).

[121] Wimmer E., Krakauer H., Weinert M., & Freeman A. J., (1981), “Full-potential Self-consistent Linearized-augmented-plane-wave Method For Calculating The Electronic Structure Of Molecules And Surfaces: O2 Molecule”, Phys. Rev. B, 24.

[122] Michalicek G., (2021), “How to obtain high-quality results with Fleur”, FLEUR hands-on, 12-16 April.

[123] Michalicek G., (2021), “The all-electron full-potential linearized augmented plane-wave method”, FLEUR hands-on, 12-16 April.

[124] Friedrich C., Schindlmayr A., & Blügel S., (2009), “Efficient Calculation Of The Coulomb Matrix And Its Expansion Around k=0 Within The FLAPW Method”, Comput. Phys. Commun., 180, 347–59.

[125] Marzari N., & Vanderbilt D., (1997), “Maximally-localized Generalized Wannier Functions For Composite Energy Bands”, Physics Review B, 56.

[126] Marzari N., Mostofi A. A., Yates J. R., Souza I., & Vanderbilt D., (2012), “Maximally localized Wannier functions: Theory and applications”, Rev. Mod. Phys., 84, 1419–75.

[127] Hamann D. R., & Vanderbilt D., (2009), “Maximally-localized Wannier Functions For GW Quasiparticles”, Physics Review B, 79.

[128] Aull T., Şaşıoğlu E., Maznichenko I. V., Ostanin S., Ernst A., Mertig I., & Galanakis I., (2019), “Ab initio design of quaternary Heusler compounds for reconfigurable magnetic tunnel diodes and transistors”, Phys. Rev. Mater., 3.

BIOGRAPHY

Kübra Nur Kalkan, In 2021 she completed her undergraduate studies in Physics at Middle East Technical University, Ankara. She started her master degree in Physics studies at Gebze Technical University.

APPENDICES

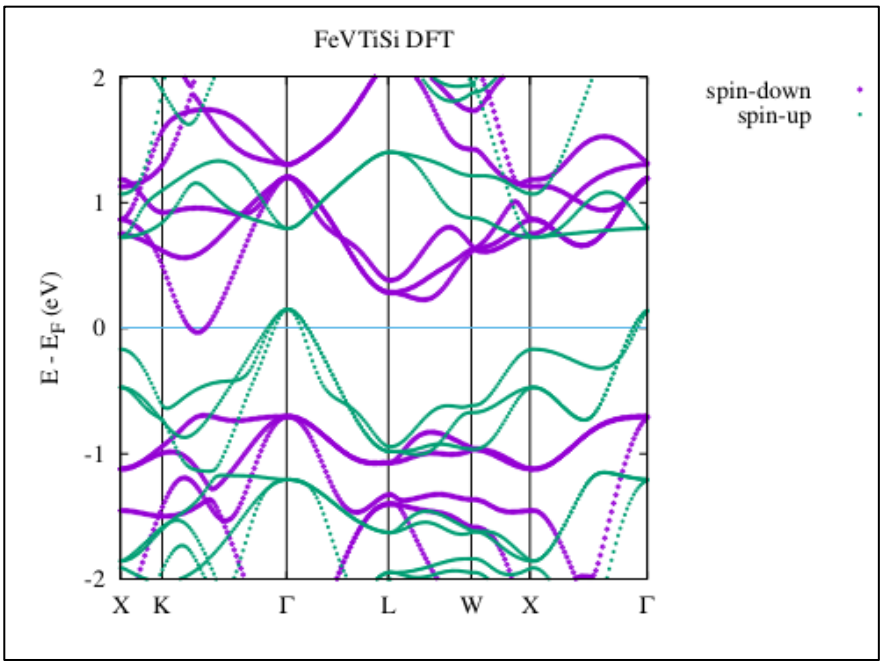

A 1 FeVTiSi, spin-resolved band diagram.

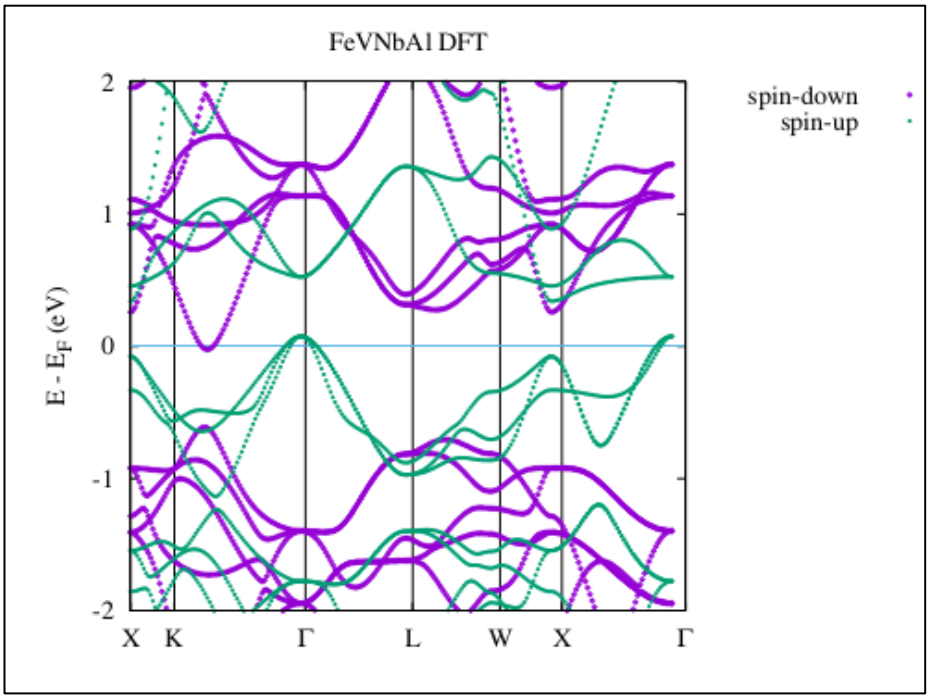

A 2 FeVNbAl spin-polarized band structure

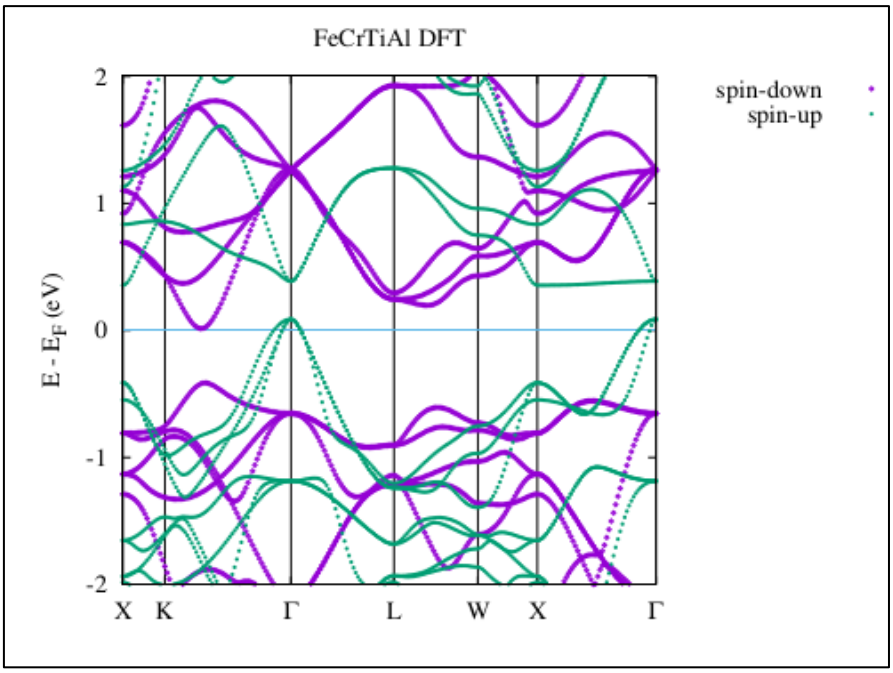

A 3 FeCrTiAl energy band diagram

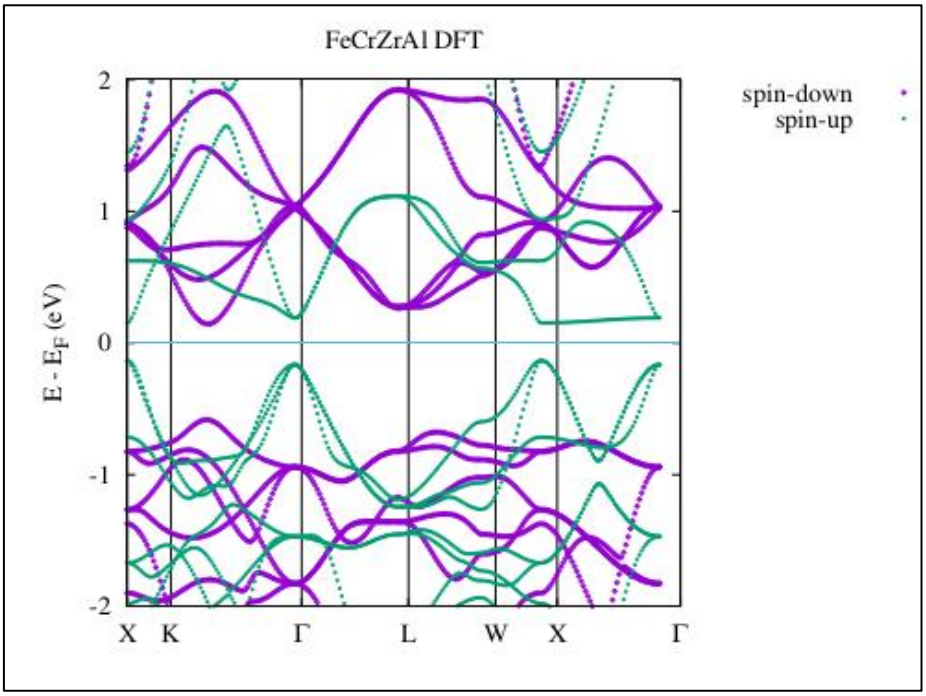

A 4 FeCrZrAl spin-polarized band structure

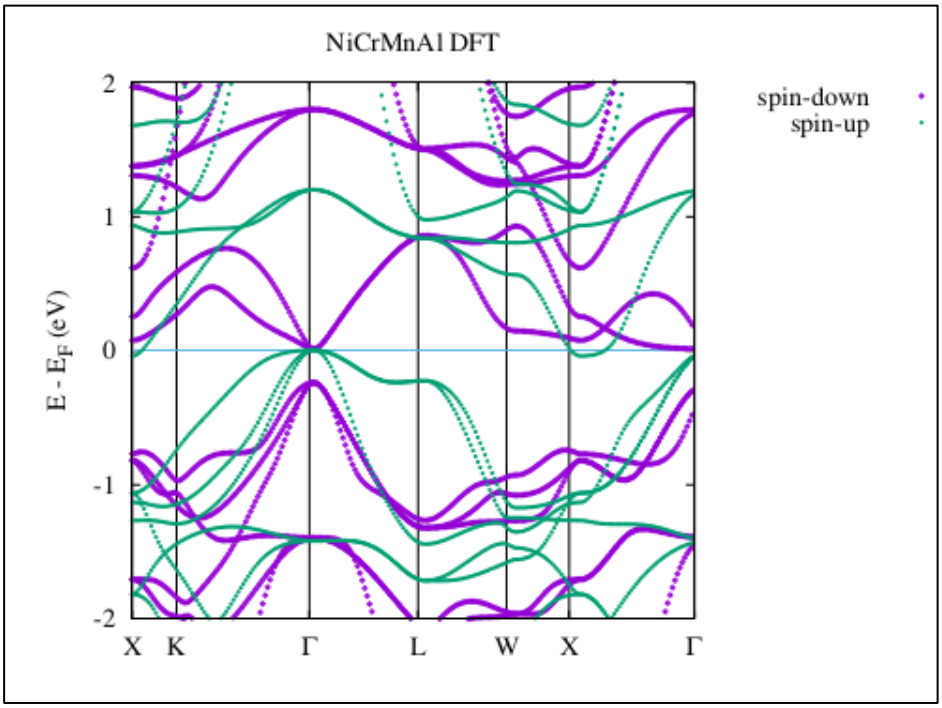

A 5 NiCrMnAl spin-resolved energy band diagram

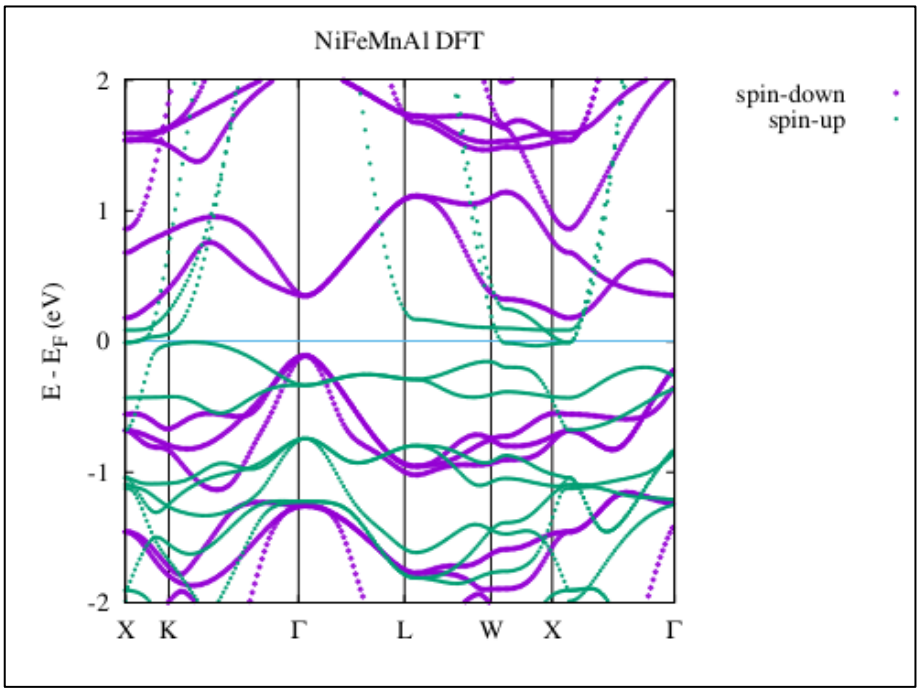

A 6 NiFeMnAl spin-polarized energy band diagram